This article has been accepted for publication in IEEE Transactions on Signal Processing. This is the author's version which has not been fully edited and content may change prior to final publication. Citation information: DOI 10.1109/TSP.2024.3384750



# Detection of Ghost Targets for Automotive Radar in the Presence of Multipath

Le Zheng, *Senior Member*, *IEEE*, Jiamin Long, Marco Lops, *Fellow*, *IEEE*
Fan Liu, *Senior Member*, *IEEE*, Xueyao Hu, Chuanhao Zhao

***Abstract*—Colocated multiple-input multiple-output (MIMO) technology has been widely used in automotive radars as it provides accurate angular estimation of the objects with a relatively small number of transmitting and receiving antennas. Since the Direction Of Departure (DOD) and the Direction Of Arrival (DOA) of *line-of-sight* targets coincide, MIMO signal processing allows for the formation of a larger virtual array for angle finding. However, multiple paths impinging the receiver is a major limiting factor, in that radar signals may bounce off obstacles, creating echoes for which the DOD does not equal the DOA. Thus, in complex scenarios with multiple scatterers, the direct paths of the intended targets may be corrupted by indirect paths from other objects, which leads to inaccurate angle estimation or ghost targets. In this paper, we focus on detecting the presence of ghosts due to multipath by regarding it as the problem of deciding between a *composite* hypothesis, $\mathcal{H}_0$ say, that the observations only contain an unknown number of direct paths sharing the same (unknown) DOD's and DOA's, and a *composite* alternative, $\mathcal{H}_1$ say, that the observations also contain an unknown number of indirect paths, for which DOD's and DOA's do not coincide. We exploit the Generalized Likelihood Ratio Test (GLRT) philosophy to determine the detector structure, offering closed-form expressions for theoretical detection performance, and a convex waveform optimization approach to improve detection performance. In practical scenarios, the unknown parameters of GLRT philosophy are replaced by carefully designed estimators. The angles of both the active direct paths and of the multi-paths are indeed estimated through a sparsity-enforced Compressed Sensing (CS) approach with Levenberg-Marquardt (LM) optimization to estimate the angular parameters in the continuous domain. Simulation and experimental results are finally offered in order to validate the proposed solution.**

***Index Terms*—Automotive radar, Colocated multiple-input multiple-output (MIMO), multipath, GLRT, group sparse.**

This work was supported in part by the National Natural Science Foundation of China (Grant No.62388102); The work of M. Lops was supported by the European Union, under the Italian National Recovery and Resilience Plan (PNRR) of Next Generation EU, through the "Telecommunications of the Future" (PE00000001 – program "RESTART" – E63C22002040007); (*Corresponding author: Xueyao Hu*).

Le Zheng, Jiamin Long, Xueyao Hu and Chuanhao Zhao are with the School of Information and Electronics, Beijing Institute of Technology, Beijing 100081, China, and with the Chongqing Innovation Center, Beijing Institute of Technology, Chongqing 401120, China. Xueyao Hu is also with the Electromagnetic Sensing Research Center of CEMEE State Key Laboratory, Beijing 100081, China. (e-mail:le.zheng.cn@gmail.com, jiaminlong0548@163.com, xueyao.hu@qq.com, 13041258366@163.com).

Marco Lops is with the Department of Electrical and Information Technology (DIETI), University of Naples Federico II, 80138 Naples, Italy, and also with the Consorzio Nazionale Interuniversitario per le Telecomunicazioni, 43124 Parma, Italy (e-mail: lops@unina.it).

Fan Liu is with the Department of Electronic and Electrical Engineering, Southern University of Science and Technology, Shenzhen 518055, China (e-mail: liuf6@sustech.edu.cn).

## I. Introduction

In recent years, the need for safer driving has led to a significant demand for automotive radar [1]–[4]. Colocated multiple-input multiple-output (MIMO) technology has been proven to be effective in providing accurate angular estimation of objects with a relatively small number of antennas, making it popular in the automotive industry [5]–[7].

One major challenge of colocated MIMO systems is the multipath reflection, where the target's echo takes multiple paths to reach the receiver, including direct and indirect paths [8]–[11]. Direct paths involve the signal being transmitted from the radar to the target and then reflected back to the radar directly, while the indirect paths could bounce multiple times between reflectors. Usually, due to different propagation delays, range gating can get rid of the indirect paths from the target we are trying to detect. However, the direction of departure (DOD) of the signal does not equal the direction of arrival (DOA) for some indirect paths, [5], [12], so the assumption of colocated MIMO does not hold. As a consequence, in multi-target scenarios, the direct paths of intended targets may be corrupted by indirect paths from other objects, and applying classical angle finding algorithms may result in degraded angle estimation accuracy and detection of ghost targets.

To detect ghost targets, some researchers exploit the geometrical relationships of the detections in the delay-Doppler domain. Specifically, R. Feng et al. employed the Hough transform to explore the linear relationship of the multipath detections [13]. F. Ross et al. detected the ghost targets by analyzing the Doppler distribution of moving targets [14]. These methods can be effective when the speed of the ghost target is significant, and the efficient utilization of Doppler information can aid in extracting geometric information from multipaths for identification. Notably, the authors in [15] proposed a novel method to suppress ghosts through waveform design, which effectively controls the responses of distinct delay-Doppler cells with a high degree of precision. However, in situations with densely distributed objects, ghost targets with low speeds may couple with the stationary objects, making it difficult to use Doppler information to identify them.

Several strategies for multipath ghost suppression in the angular domain have been proposed so far, ranging from antenna design [9], [16] to synthetic aperture radar (SAR) [17] and deep learning [18]. Alternative deep neural network (DNN) [19] method seeks to verify DOD and DOA equality but may overlook complexities from mixed paths within a delay-Doppler cell. Considering the potential advantages of indirect paths in non-line-of-sight detection [20], [21] or reconfigurable intelligent surface (RIS) applications [22], accurately detecting and estimating the parameters of each path is more valuable than simply suppressing multipath: this is the idea underlying [23], where the presence of multipath reflections is detected through a Generalized Likelihood Ratio Test (GLRT). The detector was developed under a specific signal model where only two TX antennas are used and all indirect paths for a target are confined to a single delay-Doppler cell. However, in automotive radars, MIMO arrays typically incorporate more TX antennas [24] and a single delay-Doppler cell can contain paths from multiple targets. Given the potential model mismatch, the performance of angle estimation in [23] degrades in such situations and the GLRT would fail.

Accurate estimation of target information is crucial for ghost detection in the angular domain, particularly in scenarios involving mixed first-order and direct paths. The coexistence of these paths often results in significant mutual interference, while discrepancies in DOD and DOA for indirect paths further complicate estimations, posing a challenge to achieving high accuracy angle measurements. In the field of bistatic MIMO radar, the angle finding methods for situations with different DOA and DOD have been widely studied. Subspace methods, such as the two-dimensional multiple signal classification (2D-MUSIC) [25] and unitary-estimation of signal parameters via rotational invariance technique (U-ESPRIT) [26] have been proposed. These methods have limitations related to signal and noise characteristics, array geometry, and computational complexity, which make them unsuitable for automotive radars. In [27], minimum variance distortionless response (MVDR) is utilized for spectrum estimation, addressing grating lobes in sparse MIMO radar by proposing a suppression method tailored for multipath environments. In [28], an iterative adaptive approach (IAA) was employed to estimate the two-dimensional spatial spectrum for automotive radar, while in [29], the authors propose a joint direction of departure (DOD) and direction of arrival (DOA) estimation method by comparing the power distribution of the IAA spectrum. More recent techniques based on compressed sensing (CS) theory [30] provide an alternative for jointly estimating the DOD and DOA [31], [32]. The performance of these methods depends on the designed dictionaries and gridding scheme in the angular domain. However, as the paths are usually specified by parameters in a continuous domain, the discretization usually leads to model mismatch and degradation in estimation [33], [34].

In this paper, we further investigate ghost target detection in the angular domain, to the end of detecting the indirect paths and allowing their removal, so as to preserve only the direct paths from the target. Two types of paths are considered in our analysis: direct paths, exhibiting the same DOD and DOA, and first-order paths (more on this in Section II) whose DOD does not equal DOA. After deriving the MIMO radar signal model, the problem of first-order paths existence is stated as a binary decision problem between a composite hypothesis, $\mathcal{H}_0$ say, that the observations only contain an unknown number of direct paths sharing the same (unknown) DOD's and DOA's, and a *composite* alternative, $\mathcal{H}_1$ say, that the observations also contain an unknown number of indirect paths, for which DOD's and DOA's do not coincide. In this context, we resort to the GLRT philosophy to determine the detector structure and propose a convex waveform optimization approach to enhance detection performance. As for the implementable solution, the unknown parameters of GLRT philosophy are replaced by carefully designed estimators. In particular, to estimate the angle of the paths under the two alternative hypotheses, we develop CS methods in the continuous domain for the cases with and without first-order paths, respectively. Specifically, in the situation with first-order paths, the algorithm is designed with a group-sparsity enforced structure to take advantage of the reversibility of the propagation path. To improve the convergence performance, we adopt a Levenberg-Marquardt (LM) optimization approach to accelerate the execution of the algorithm. The proposed method has shown superior performance over existing methods by simulation. An extensive performance assessment is finally offered in order to validate the proposed strategy.

The remainder of the paper is organized as follows: In Section II, we present the signal model of multipath reflection. Section III details the proposed detector and derives its exact theoretical performance. In Section IV, we describe the proposed angle estimation methods under different situations. In Section V, we present the simulation results, and finally, Section VI concludes the paper.

*Notation* : The transposition, Hermitian transposition, inversion, pseudo-inversion, Kronecker product, Khatri-Rao (KR) product, Hadamard product and direct sum operations are denoted by $(\cdot)^T$, $(\cdot)^H$, $(\cdot)^{-1}$, $(\cdot)^\dagger$, $\otimes$, $\circ$, $\odot$, $\oplus$, respectively. Matrix $\mathbf{X}$ and vector $\mathbf{x}$ are indicated in boldface. The notation $\mathrm{diag}(\mathbf{X})$ denotes the operation of extracting elements from the diagonal of $\mathbf{X}$ to form a new vector. $\|\mathbf{x}\|_2 = \sqrt{\sum_i x_i^2}$ denotes the $\ell_2$-norm. $\mathcal{R}(\mathbf{X})$ denote the range-span of the matrix $\mathbf{X}$. $\mathbf{x}^{(k)}$ denotes the value of $\mathbf{x}$ at the $k$-th iteration and $\mathbf{x}^{(k,j)}$ denotes the value of $\mathbf{x}^{(k)}$ at the $j$-th iteration. $\boldsymbol{I}_n$ being the $n \times n$ identity matrix. For $\mathbf{X}$ , the $n$-th column vector and $(m,n)$-th element are denoted by $\mathbf{X}(n)$ and $[\mathbf{X}]_{m,n}$, respectively, while the $m$-th element of vector $\mathbf{x}$ is given by $[\mathbf{x}]_m$ .

## II. Signal Model and Problem Formulation

State-of-the-art automotive radars usually employ Frequency Modulated Continuous Wave (FMCW) sequences to enable high-resolution estimation of target range and radial velocity [35], [36], and adopt colocated MIMO technology to synthesize a large virtual array for accurate angle estimation using multiple transmit and receive antennas. We consider a colocated MIMO radar system with $M_T$ transmit antennas emitting as many coded sequences [37] and $M_R$ receive antennas. At the receiver end, the signal at each antenna undergoes the usual processing to extract the contribution of each transmit antenna and synthesize a MIMO channel with $M_T M_R$ elements. This signal is then processed via fast Fourier transform (FFT) along fast and slow time to obtain the delay-Doppler profile of the echo path [1]. Finally, the virtual array response of the detected target can be constructed to estimate the direction of targets [6].

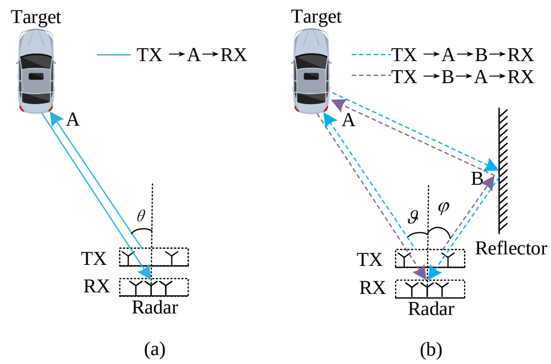


Fig. 1: (a) A direct path, (b) A pair of first-order paths.

The multipath scenario can be visualized as a radar emitting signals that bounce off a target and a reflector. As depicted in Fig. 1, where the target is placed at position A and the reflector is located at point B, the signals received by the radar can take different paths as follows:

- *Direct path*: The shortest path between the radar and the target, where the departure and arrival angles of the direct path are equal to the target angle as shown in Fig. 1a.
- *First-order paths*: The indirect paths involve a single bounce at the reflector on the way of departure or arrival, resulting in a longer delay compared to the direct path. As shown in Fig. 1 b, the DOD's of the first-order paths do not equal the respective DOA's.
- *Higher-order paths*: The indirect paths involve more bounces before the echo reaches the receiver. However, due to the attenuation caused by scattering at the target and reflectors, higher-order paths are normally weak, and may thus be neglected [13], [38].

In automotive radar, delay and Doppler information of direct path yields target range and velocity [2], respectively. Both DOD and DOA equal the angle of far-field targets, enabling the virtual array to form an aperture larger than the physical aperture of the radar, thereby enhancing angular resolution and accuracy of angle estimation [5], [24], [39]. Although Fig. 1 depicts, for simplicity reasons, a single target scenario, the situation we consider here is one wherein multiple reflecting objects are present in the radar field of view, whereby the direct paths generated by the intended targets may end up being corrupted by the first-order paths generated by other reflecting objects.

Consider a FMCW MIMO radar that transmits $L$ pulses from each transmit antenna and exploits slow-time coding as a multiplexing approach. Denote $\mathbf{x}(l) = [x_1(l), x_2(l), \cdots, x_{M_T}(l)]^T$ as the vector of the code transmitted at the $l$-th epoch by the $M_T$ transmit antennas, the transmitted code matrix can be represented as $\mathbf{X} = [\mathbf{x}(1), \mathbf{x}(2), \cdots, \mathbf{x}(L)] \in \mathbb{C}^{M_T \times L}$. After performing FFT on the fast-time of received measurements, we consider $K_0$ direct paths and $K_1$ pairs of first-order paths in a given delay cell under test and model the observation $\boldsymbol{y}(l) \in \mathbb{C}^{M_R \times 1}$ as

$$\begin{aligned}\boldsymbol{y}(l) = &\sum_{k=1}^{K_0} \alpha_k e^{j2\pi f_d (l-1)} \mathbf{a}_R(\theta_k) \mathbf{a}_T^T(\theta_k) \mathbf{x}(l) \\ &+ \sum_{k=1}^{K_1} \beta_{k,1} e^{j2\pi f_d (l-1)} \mathbf{a}_R(\varphi_k) \mathbf{a}_T^T(\vartheta_k) \mathbf{x}(l) \\ &+ \sum_{k=1}^{K_1} \beta_{k,2} e^{j2\pi f_d (l-1)} \mathbf{a}_R(\vartheta_k) \mathbf{a}_T^T(\varphi_k) \mathbf{x}(l) + \mathbf{w}(l),\end{aligned} \tag{1}$$

where

- $\alpha_k$, $\beta_{k,1}$ and $\beta_{k,2}$ represent the complex amplitude of the $k$-th direct path for $k = 1, 2, \ldots, K_0$ and the $k$-th pair first-order paths for $k = 1, 2, \ldots, K_1$ respectively. The amplitudes depend on a number of factors such as the transmit power, antenna gain pattern, path loss propagation, reflection coefficient, and matched-filter gain.
- $\theta_k$ denotes the DOD of the $k$-th direct path, which is equal to the DOA; $\vartheta_k$ and $\varphi_k$ denote the DOD and DOA of the $k$-th pair first-order path with $\vartheta_k \neq \varphi_k$; $f_d$ is the normalized Doppler frequency.
- $\mathbf{a}_T(\cdot) \in \mathbb{C}^{M_T \times 1}$ and $\mathbf{a}_R(\cdot) \in \mathbb{C}^{M_R \times 1}$ are the steering vectors

$$\begin{aligned}\mathbf{a}_T(\theta) = \frac{1}{\sqrt{M_T}} \Big[ & e^{j2\pi d_{T,1} \sin(\theta)/\lambda}, e^{j2\pi d_{T,2} \sin(\theta)/\lambda}, \ldots \\ & , e^{j2\pi d_{T,M_T} \sin(\theta)/\lambda} \Big]^T,\end{aligned} \tag{2}$$

$$\begin{aligned}\mathbf{a}_R(\phi) = \frac{1}{\sqrt{M_R}} \Big[ & e^{j2\pi d_{R,1} \sin(\phi)/\lambda}, e^{j2\pi d_{R,2} \sin(\phi)/\lambda}, \ldots \\ & , e^{j2\pi d_{R,M_R} \sin(\phi)/\lambda} \Big]^T,\end{aligned} \tag{3}$$

  with $\theta$ and $\phi$ denoting the angles of $\mathbf{a}_T(\cdot)$ and $\mathbf{a}_R(\cdot)$, respectively, $\lambda$ denoting the wavelength, $d_{T,m}$ and $d_{R,n}$ denoting the relative distances of the $m$-th TX element and the $n$-th RX element from the reference array element.
- $\mathbf{w}(l) \in \mathbb{C}^{M_R \times 1}$ is the white Gaussian noise at the radar receive array, distributed as $\mathcal{CN}(\mathbf{0}, \sigma^2 \boldsymbol{I}_{M_R})$, with $\sigma^2$ denoting the noise variance [40].

Denoting $\mathbf{P}(f_d) = \mathrm{diag}\left([1, e^{j2\pi f_d}, \cdots, e^{j2\pi f_d (L-1)}]\right)$, the received data matrix reads

$$\begin{aligned}\boldsymbol{Y} &= [\boldsymbol{y}(1), \boldsymbol{y}(2), \cdots, \boldsymbol{y}(L)] \\ &= \sum_{k=1}^{K_0} \alpha_k \mathbf{a}_R(\theta_k) \mathbf{a}_T^T(\theta_k) \mathbf{X} \mathbf{P}(f_d) \\ &\quad + \sum_{k=1}^{K_1} \beta_{k,1} \mathbf{a}_R(\varphi_k) \mathbf{a}_T^T(\vartheta_k) \mathbf{X} \mathbf{P}(f_d) \\ &\quad + \sum_{k=1}^{K_1} \beta_{k,2} \mathbf{a}_R(\vartheta_k) \mathbf{a}_T^T(\varphi_k) \mathbf{X} \mathbf{P}(f_d) + \boldsymbol{W},\end{aligned} \tag{4}$$

This article has been accepted for publication in IEEE Transactions on Signal Processing. This is the author's version which has not been fully edited and content may change prior to final publication. Citation information: DOI 10.1109/TSP.2024.3384750



where $\boldsymbol{W} = [\mathbf{w}(1), \mathbf{w}(2), \cdots, \mathbf{w}(L)]$. Plain matched filtering thus yields

$$\begin{aligned} \boldsymbol{Z} &= \boldsymbol{Y}(\mathbf{X}\mathbf{P}(f_d))^H \\ &= \sum_{k=1}^{K_0} \alpha_k \mathbf{a}_R(\theta_k)\mathbf{a}_T^T(\theta_k)\mathbf{X}\mathbf{P}(f_d)\mathbf{P}^H(f_d)\mathbf{X}^H \\ &\quad + \sum_{k=1}^{K_1} \beta_{k,1}\mathbf{a}_R(\varphi_k)\mathbf{a}_T^T(\vartheta_k)\mathbf{X}\mathbf{P}(f_d)\mathbf{P}^H(f_d)\mathbf{X}^H \\ &\quad + \sum_{k=1}^{K_1} \beta_{k,2}\mathbf{a}_R(\vartheta_k)\mathbf{a}_T^T(\varphi_k)\mathbf{X}\mathbf{P}(f_d)\mathbf{P}^H(f_d)\mathbf{X}^H \\ &\quad + \boldsymbol{W}\mathbf{P}^H(f_d)\mathbf{X}^H, \end{aligned} \tag{5}$$

where $\mathbf{P}(f_d)\mathbf{P}^H(f_d) = \boldsymbol{I}_L$. Vectorizing the matrix $\boldsymbol{Z}$ finally yields the general model of the virtual MIMO array signal in a given delay-Doppler cell under test, denoted as

$$\begin{aligned} \boldsymbol{z} &= (\mathbf{R}_x \otimes \boldsymbol{I}_{M_R}) \sum_{k=1}^{K_0} \alpha_k \mathbf{a}_T(\theta_k) \otimes \mathbf{a}_R(\theta_k) \\ &\quad + (\mathbf{R}_x \otimes \boldsymbol{I}_{M_R}) \sum_{k=1}^{K_1} \beta_{k,1}\mathbf{a}_T(\vartheta_k) \otimes \mathbf{a}_R(\varphi_k) \\ &\quad + (\mathbf{R}_x \otimes \boldsymbol{I}_{M_R}) \sum_{k=1}^{K_1} \beta_{k,2}\mathbf{a}_T(\varphi_k) \otimes \mathbf{a}_R(\vartheta_k) \\ &\quad + \mathbf{r}, \end{aligned} \tag{6}$$

where $\mathbf{R}_x = \mathbf{X}^*\mathbf{X}^T$, $\mathbf{r} = ((\mathbf{X}^*\mathbf{P}(f_d)) \otimes \boldsymbol{I}_{M_R})\,\tilde{\mathbf{w}}$, $\tilde{\mathbf{w}} = \mathrm{vec}(\mathbf{W})$. Denoting $\boldsymbol{\Theta}_0 = [\theta_1, \theta_2, \ldots, \theta_{K_0}]^T \in \mathbb{R}^{K_0 \times 1}$ as the vector containing the angles of $K_0$ direct paths, the corresponding steering matrix is $\mathbf{A}(\boldsymbol{\Theta}_0) = [\mathbf{a}(\theta_1), \mathbf{a}(\theta_2), \ldots, \mathbf{a}(\theta_{K_0})] \in \mathbb{C}^{M_T M_R \times K_0}$ where $\mathbf{a}(\cdot) = \mathbf{a}_T(\cdot) \otimes \mathbf{a}_R(\cdot)$. In the absence of first-order paths ($K_1 = 0$), the signal model in (6) simplifies to

$$\boldsymbol{z} = (\mathbf{R}_x \otimes \boldsymbol{I}_{M_R})\,\mathbf{A}(\boldsymbol{\Theta}_0)\boldsymbol{\alpha} + \mathbf{r}, \tag{7}$$

where $\boldsymbol{\alpha} = [\alpha_1, \alpha_2, \ldots, \alpha_{K_0}]^T \in \mathbb{C}^{K_0 \times 1}$ is the amplitude vector of direct paths.

In the presence of first-order paths ($K_1 \neq 0$), we define the DOD angle vector $\boldsymbol{\Theta}_1 = [\vartheta_1, \vartheta_2, \ldots, \vartheta_{K_1}]^T \in \mathbb{R}^{K_1 \times 1}$, the DOA angle vector $\boldsymbol{\Phi}_1 = [\varphi_1, \varphi_2, \ldots, \varphi_{K_1}]^T \in \mathbb{R}^{K_1 \times 1}$ and the amplitude vector $\boldsymbol{\beta}_1 = [\beta_{1,1}, \beta_{2,1}, \ldots, \beta_{K_1,1}, \beta_{1,2}, \beta_{2,2}, \ldots, \beta_{K_1,2}]^T \in \mathbb{C}^{2K_1 \times 1}$ for the $K_1$ pair of first-order paths. Moreover, we define $\boldsymbol{\Theta} = [\boldsymbol{\Theta}_1^T, \boldsymbol{\Phi}_1^T, \boldsymbol{\Theta}_0^T]^T \in \mathbb{R}^{(2K_1+K_0)\times 1}$, $\boldsymbol{\Phi} = [\boldsymbol{\Phi}_1^T, \boldsymbol{\Theta}_1^T, \boldsymbol{\Theta}_0^T]^T \in \mathbb{R}^{(2K_1+K_0)\times 1}$. Denoting $\mathbf{A}_T$ and $\mathbf{A}_R$ as steering matrices of the radar TX and RX arrays, respectively, we have

$$\begin{aligned} \mathbf{A}_T(\boldsymbol{\Theta}) = [&\mathbf{a}_T(\vartheta_1), \ldots, \mathbf{a}_T(\vartheta_{K_1}), \mathbf{a}_T(\varphi_1), \ldots, \mathbf{a}_T(\varphi_{K_1}), \\ &\mathbf{a}_T(\theta_1), \ldots, \mathbf{a}_T(\theta_{K_0})], \\ \mathbf{A}_R(\boldsymbol{\Phi}) = [&\mathbf{a}_R(\varphi_1), \ldots, \mathbf{a}_R(\varphi_{K_1}), \mathbf{a}_R(\vartheta_1), \ldots, \mathbf{a}_R(\vartheta_{K_1}), \\ &\mathbf{a}_R(\theta_1), \ldots, \mathbf{a}_R(\theta_{K_0})], \end{aligned}$$

and the signal model (6) can be rewritten as

$$\boldsymbol{z} = (\mathbf{R}_x \otimes \boldsymbol{I}_{M_R})\,\mathbf{A}(\boldsymbol{\Theta}, \boldsymbol{\Phi})\boldsymbol{\beta} + \mathbf{r}, \tag{8}$$

In the previous equation $\mathbf{A}(\boldsymbol{\Theta}, \boldsymbol{\Phi}) = \mathbf{A}_T(\boldsymbol{\Theta}) \circ \mathbf{A}_R(\boldsymbol{\Phi})$ denotes the response matrix, $\boldsymbol{\beta} = [\boldsymbol{\beta}_1^T, \boldsymbol{\alpha}^T]^T \in \mathbb{C}^{(2K_1+K_0)\times 1}$ is the complex amplitude vector. Note that a pair of first-order paths share the same sparse pattern which is usually smaller than the number of array elements [23], resulting in a group-sparse structure that can be employed for multipath estimation purpose.

## III. Detection of Multipath

In the general setup outlined in the previous section, ghost detection amounts to solving a coupled detection-estimation problem, wherein we have to discriminate between a composite hypothesis, $\mathcal{H}_0$ say, that the observations only contain a *unknown* number $K_0$ of direct paths coming from as many *unknown* different directions, against a *composite* alternative, $\mathcal{H}_1$ say, that the observations also contain a *unknown* number $K_1$ of first-order paths each characterized by an unknown pair of angles. In what follows, we (suboptimally) break up this problem into a two-step procedure: first, we introduce and discuss a GLRT assuming that the number of the direct and first-order paths, as well as the corresponding angular information - i.e., the matrices $\mathbf{A}(\boldsymbol{\Theta}_0)$ of (7) and $\mathbf{A}(\boldsymbol{\Theta}, \boldsymbol{\Phi})$ of (8) - are *known*. Subsequently, we illustrate a number of possible techniques to provide the detector with the required information (i.e., we make it *implementable*), by formulating the problem of preliminary estimating these matrices as a sparse recovery problem taking full advantage of the models introduced in the previous section.

### A. GLRT detector

Assume at first that the two matrices in (7) and (8) are known, whereby we have to solve the *composite* binary hypothesis test

$$\begin{cases} \mathcal{H}_0 : \boldsymbol{z} = (\mathbf{R}_x \otimes \boldsymbol{I}_{M_R})\mathbf{A}(\boldsymbol{\Theta}_0)\boldsymbol{\alpha} + \mathbf{r}, \\ \mathcal{H}_1 : \boldsymbol{z} = (\mathbf{R}_x \otimes \boldsymbol{I}_{M_R})\mathbf{A}(\boldsymbol{\Theta}, \boldsymbol{\Phi})\boldsymbol{\beta} + \mathbf{r}, \end{cases} \tag{9}$$

where $\boldsymbol{\alpha} \in \mathbb{C}^{K_0 \times 1}$ and $\boldsymbol{\beta} \in \mathbb{C}^{(K_0+2K_1)\times 1}$ are *unknown* parameters. Before proceeding, it is worth commenting on some constraints we want to force upon the solution of the above test, i.e.:

1) We want the test to be Constant False Alarm Rate (CFAR), i.e. its test statistic pdf under $\mathcal{H}_0$ *and* its detection threshold to be *functionally independent* of the noise floor *and* of the directions and intensities of the direct paths;
2) We want the resulting test to have some form of *optimality*, so as to use its performance as a yardstick to compare our implementable solutions to.

Since

$$\begin{aligned} \mathbb{E}(\mathbf{r}\mathbf{r}^H) &= \mathbb{E}\left((\mathbf{X}^* \otimes \boldsymbol{I}_{M_R})\tilde{\mathbf{w}}\tilde{\mathbf{w}}^H(\mathbf{X}^* \otimes \boldsymbol{I}_{M_R})^H\right) \\ &= (\mathbf{X}^* \otimes \mathbf{I}_{M_R})\sigma^2\boldsymbol{I}_{M_R L}(\mathbf{X}^T \otimes \boldsymbol{I}_{M_R}) \\ &= \sigma^2(\mathbf{X}^*\mathbf{X}^T) \otimes \boldsymbol{I}_{M_R} \\ &= \sigma^2\mathbf{R}_x \otimes \boldsymbol{I}_{M_R}, \end{aligned} \tag{10}$$

This article has been accepted for publication in IEEE Transactions on Signal Processing. This is the author's version which has not been fully edited and content may change prior to final publication. Citation information: DOI 10.1109/TSP.2024.3384750



we have $\mathbf{r} \sim \mathcal{CN}(\mathbf{0}, \sigma^2\mathbf{\Sigma}_x)$ where $\mathbf{\Sigma}_x = \mathbf{R}_x \otimes \boldsymbol{I}_{M_R}$. From now on, we assume $\mathrm{rank}(\mathbf{R}_x) = \mathrm{rank}(\mathbf{X}) = M_T$ [1], the correlation matrix $\mathbf{\Sigma}_x$ is also full-rank. Since $\mathbf{\Sigma}_x$ is known, a noise-whitening transformation converts the test (9) into

$$\begin{aligned} H_0 : &\bar{\boldsymbol{z}} \sim \mathcal{CN}(\mathbf{\Sigma}_x^{1/2}\mathbf{A}(\mathbf{\Theta}_0)\boldsymbol{\alpha}, \sigma^2\boldsymbol{I}_{M_TM_R}),\\ H_1 : &\bar{\boldsymbol{z}} \sim \mathcal{CN}(\mathbf{\Sigma}_x^{1/2}\mathbf{A}(\mathbf{\Theta},\mathbf{\Phi})\boldsymbol{\beta}, \sigma^2\boldsymbol{I}_{M_TM_R}), \end{aligned} \tag{11}$$

where $\bar{\boldsymbol{z}} = \mathbf{\Sigma}_x^{-1/2}\boldsymbol{z}$. Notice that, by construction, $\mathbf{\Sigma}_x^{1/2}\mathbf{A}(\mathbf{\Theta},\mathbf{\Phi})$ is the matrix concatenation [41]

$$\mathbf{\Sigma}_x^{1/2}\mathbf{A}(\mathbf{\Theta},\mathbf{\Phi}) = \mathbf{\Sigma}_x^{1/2}[\boldsymbol{E}\ , \mathbf{A}(\mathbf{\Theta}_0)], \tag{12}$$

where $\boldsymbol{E} = [\mathbf{A}(\mathbf{\Theta}_1,\mathbf{\Phi}_1), \mathbf{A}(\mathbf{\Phi}_1,\mathbf{\Theta}_1)] \in \mathbb{C}^{M_TM_R\times 2K_1}$ only depends on the DODs and the DOAs of the first-order paths. Under the CFAR constraint outlined above, we are thus in the situation of detecting a subspace signal in subspace interference and noise of unknown level [41, Section VIII], whereby the GLRT reads

$$\mathcal{T}_{GLRT} = \frac{\|\boldsymbol{P}(\mathbf{\Theta}_0)\bar{\boldsymbol{z}}\|^2}{\|\boldsymbol{P}(\mathbf{\Theta},\mathbf{\Phi})\bar{\boldsymbol{z}}\|^2} \underset{\mathcal{H}_0}{\overset{\mathcal{H}_1}{\gtrless}} \lambda_G, \tag{13}$$

where $\boldsymbol{P}(\mathbf{\Theta}_0) = \boldsymbol{I}_{M_TM_R} - \mathbf{\Sigma}_x^{1/2}\mathbf{A}(\mathbf{\Theta}_0)(\mathbf{\Sigma}_x^{1/2}\mathbf{A}(\mathbf{\Theta}_0))^{\dagger} = \mathbf{P}_0$ is the orthogonal projector onto the orthogonal complement of $\mathbf{\Sigma}_x^{1/2}\mathbf{A}(\mathbf{\Theta}_0)$ in $\mathbb{C}^{M_TM_R}$, and $\boldsymbol{P}(\mathbf{\Theta},\mathbf{\Phi}) = \boldsymbol{P}_1$ has the same meaning with respect to $\mathbf{\Sigma}_x^{1/2}\mathbf{A}(\mathbf{\Theta},\mathbf{\Phi})$, $\lambda_G$ is the detection threshold.

The test (13), which we adopt outright, complies with the prior constraints 1) and 2). Concerning 1), indeed, the test is *invariant* to transformations that rotate the observations in the range span of $\boldsymbol{G} = \boldsymbol{P}_0\mathbf{\Sigma}_x^{1/2}\boldsymbol{E}$ and positively *scale* $\bar{\boldsymbol{z}}$ [41]. As we'll be shortly verifying, this results in a detection threshold and a false alarm probability which are independent of both $\mathbf{A}(\mathbf{\Theta_0})$ and the noise floor $\sigma^2$. Concerning optimality, the test statistic in (13) turns out to be a *maximal invariant* statistic [42], whereby the test (13) is Uniformly Most Powerful (UMP) one under the said invariance constraints.

### B. Performance bounds and waveform optimization

In this section, we first specialize on the problem at hand the key results of [41, Section VIII] concerning the detection performance of the test family (13), and then we deal with the optimization of the transmit space-time code matrix. Since $\mathbf{\Sigma}_x^{1/2}\mathbf{A}(\mathbf{\Theta},\mathbf{\Phi})$ is a concatenation of $\mathbf{\Sigma}_x^{1/2}\mathbf{A}(\mathbf{\Theta_0})$ with some $\boldsymbol{E}$, we have that $\mathcal{R}(\mathbf{\Sigma}_x^{1/2}\mathbf{A}(\mathbf{\Theta_0})) \subseteq \mathcal{R}(\mathbf{\Sigma}_x^{1/2}\mathbf{A}(\mathbf{\Theta},\mathbf{\Phi}))$, whereby $\mathcal{R}(\boldsymbol{P}_1) \subseteq \mathcal{R}(\boldsymbol{P}_0)$, i.e. $\mathcal{R}(\boldsymbol{P}_0) = \mathcal{R}(\boldsymbol{P}_1) \oplus \boldsymbol{S}_{\perp}$, where $\boldsymbol{S}_{\perp}$ denotes the orthogonal complement of $\mathcal{R}(\boldsymbol{P}_1)$ in $\mathcal{R}(\boldsymbol{P}_0)$. Denoting $\boldsymbol{P}^{\boldsymbol{S}_{\perp}}$ as the orthogonal projector onto $\boldsymbol{S}_{\perp}$, and assuming that the echo signals from different paths are incoherent, we have $\dim(\mathcal{R}(\boldsymbol{P}_1)) = M_TM_R - K_0 - 2K_1$, $\dim(\mathcal{R}(\boldsymbol{P}_0)) = M_TM_R - K_0$ and $\dim\left(\mathcal{R}\left(\boldsymbol{P}^{\boldsymbol{S}_{\perp}}\right)\right) = 2K_1$, leading to [41, Section VIII]

$$\frac{\|\boldsymbol{P}_0\bar{\boldsymbol{z}}\|^2}{\|\boldsymbol{P}_1\bar{\boldsymbol{z}}\|^2} = 1 + \frac{\left\|\boldsymbol{P}^{\boldsymbol{S}_{\perp}}\bar{\boldsymbol{z}}\right\|^2}{\|\boldsymbol{P}_1\bar{\boldsymbol{z}}\|^2} = 1 + X. \tag{14}$$

[1] A justification of this assumption will be given infra

Under $\mathcal{H}_0$, $X$ is the ratio of two independent central Chi-square random variables, with $4K_1$ and $2(M_TM_R - K_0 - 2K_1)$ degrees of freedom, respectively, and hence has a Fisher-Snedecor distribution with density

$$f_{X|\mathcal{H}_0}(x) = \frac{1}{B\left(2K_1; m\right)} x^{2K_1-1}(1+x)^{-(m+2K_1)}, \tag{15}$$

where $m = M_TM_R - K_0 - 2K_1$ and $B\left(a; b\right)$ denotes the beta function with parameters $a$ and $b$.

In order to determine the density under $\mathcal{H}_1$, a model for $\boldsymbol{\beta}$ is to be chosen. A customary assumption is that $\boldsymbol{\beta} \sim \mathcal{CN}(0, \boldsymbol{K}_{\beta})$, namely that it is a proper complex Gaussian vector with covariance matrix $\boldsymbol{K}_{\beta}$, which implies that the test statistic has again a Fisher-Snedecor distribution [41, Section VIII]. Since

$$\begin{aligned} &\mathbb{E}\left(\left\|\boldsymbol{P}^{\boldsymbol{S}_{\perp}}\bar{\boldsymbol{z}}\right\|^2|\mathcal{H}_1\right) = \mathbb{E}\left(\left\|\boldsymbol{P}^{\boldsymbol{S}_{\perp}}\mathbf{\Sigma}_x^{1/2}\mathbf{A}(\mathbf{\Theta},\mathbf{\Phi})\boldsymbol{\beta} + \boldsymbol{P}^{\boldsymbol{S}_{\perp}}\mathbf{r}\right\|^2\right)\\ &= \mathrm{Tr}\left(\boldsymbol{E}^H\mathbf{\Sigma}_x^{1/2}\boldsymbol{P}_0\mathbf{\Sigma}_x^{1/2}\boldsymbol{E}\boldsymbol{K}_{\beta}\right) + \sigma^2 2K_1, \end{aligned} \tag{16}$$

we have

$$\begin{aligned} f_{X|\mathcal{H}_1}(x) \quad = \quad &\frac{1}{(1+\rho_1)B\left(2K_1; m\right)}\left(\frac{x}{1+\rho_1}\right)^{2K_1-1}\\ &\times\left(1+\frac{x}{1+\rho_1}\right)^{-(m+2K_1)}, \end{aligned} \tag{17}$$

where

$$\rho_1 = \frac{\mathrm{Tr}\left(\boldsymbol{E}^H\mathbf{\Sigma}_x^{1/2}\boldsymbol{P}_0\mathbf{\Sigma}_x^{1/2}\boldsymbol{E}\boldsymbol{K}_{\beta}\right)}{2K_1\sigma^2}. \tag{18}$$

Elementary calculations allow thus to determine the performance of the test in the form:

$$P_{\mathrm{fa}} = 1 - \frac{1}{B\left(2K_1; m\right)}\sum_{i=0}^{m-1}\frac{(-1)^i\binom{m-1}{i}}{2K_1+i}\left(1-\frac{1}{\lambda_G}\right)^{2K_1+i}, \tag{19}$$

$$P_{\mathrm{d}} = 1 - \frac{1}{B\left(2K_1; m\right)}\sum_{i=0}^{m-1}\frac{(-1)^i\binom{m-1}{i}}{2K_1+i}\left(\frac{\lambda_G-1}{\lambda_G+\rho_1}\right)^{2K_1+i}. \tag{20}$$

As far as the false alarm performance is concerned, we recall here that the test (13) achieves CFARness, whereby $P_{\mathrm{fa}}$ only depends on $K_0$ and $K_1$: sample plots of the behavior of $P_{\mathrm{fa}}$ versus the threshold for some values of $K_0$ and $K_1$ are reported in Fig. 2.

Concerning the detection probability, we refer to the interesting special case that $\boldsymbol{\beta} \sim \mathcal{CN}(0, \sigma_{\beta}^2\boldsymbol{I}_{2K_1})$, $\boldsymbol{\alpha} \sim \mathcal{CN}(0, \sigma_{\alpha}^2\boldsymbol{I}_{K_0})$, which yields

$$\begin{aligned} \rho_1 = \frac{\sigma_{\beta}^2}{2K_1\sigma^2}\mathrm{Tr}\left(\boldsymbol{E}^H\mathbf{\Sigma}_x^{1/2}\boldsymbol{P}_0\mathbf{\Sigma}_x^{1/2}\boldsymbol{E}\right) = \frac{\sigma_{\beta}^2}{2K_1\sigma^2}\\ \times\mathrm{Tr}\left(\boldsymbol{E}^H\mathbf{\Sigma}_x\boldsymbol{E} - \boldsymbol{E}^H\mathbf{\Sigma}_x\mathbf{A}_0(\mathbf{A}_0^H\mathbf{\Sigma}_x\mathbf{A}_0)^{-1}\mathbf{A}_0^H\mathbf{\Sigma}_x\boldsymbol{E}\right), \end{aligned} \tag{21}$$

where $\mathbf{A}_0 = \mathbf{A}(\mathbf{\Theta}_0)$. The quantity in (21) represents a suitable figure of merit to be maximized over the set of admissible code matrices under additional constraints, so as to endow the resulting waveform with relevant features. The first constraint

This article has been accepted for publication in IEEE Transactions on Signal Processing. This is the author's version which has not been fully edited and content may change prior to final publication. Citation information: DOI 10.1109/TSP.2024.3384750



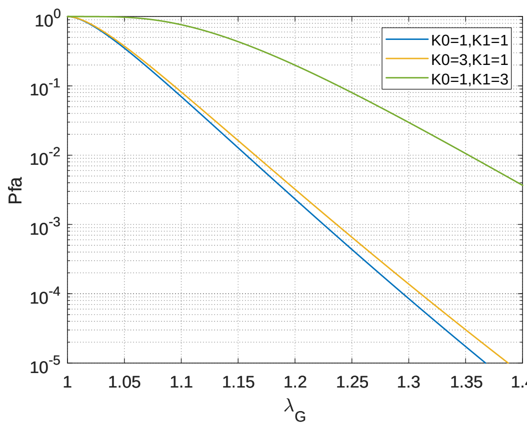


Fig. 2: $P_{\mathrm{fa}}$ versus $\lambda_G$ with $M_T M_R = 48$.

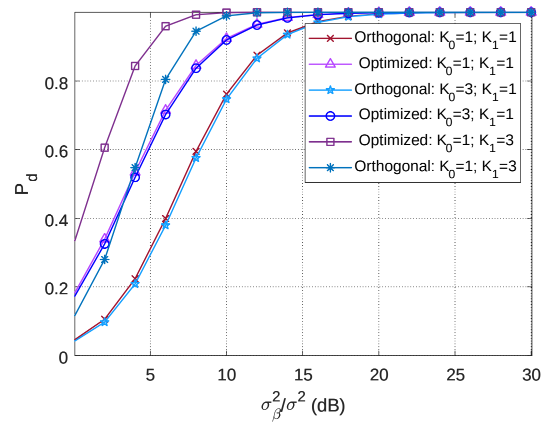


Fig. 3: $P_{\mathrm{d}}$ versus $\sigma_\beta^2/\sigma^2$ with $M_T M_R = 48$.

is obviously a power constraint, expressed as $\mathbf{x}_m^H \mathbf{x}_m = 1$, where $\mathbf{x}_m$ represents the code sequence of the $m$-th transmitter for $m = 1, 2, \ldots, M_T$. Notice also that, in the presence of some prior information on the surrounding environment, a reasonable constraint should be $\| \boldsymbol{R}_x - \boldsymbol{V} \|^2 \leq \epsilon$ where $\boldsymbol{V}$ is a proper beamforming matrix that accounts for prior information on the angular location of real and virtual sources. If no such information is available, then we need to robustify the design, by avoiding the radar has blind angles, whereby we force the condition that $\boldsymbol{R}_x$ should not be too far from the "orthogonal form" which ensures complete coverage of all the angles. As a consequence, the optimization problem to be solved reads

$$\begin{aligned}
&\max_{\boldsymbol{\Sigma}_x} \mathrm{Tr}\left(\boldsymbol{E}^H \boldsymbol{\Sigma}_x \boldsymbol{E} - \boldsymbol{E}^H \boldsymbol{\Sigma}_x \mathbf{A}_0 (\mathbf{A}_0^H \boldsymbol{\Sigma}_x \mathbf{A}_0)^{-1} \mathbf{A}_0^H \boldsymbol{\Sigma}_x \boldsymbol{E}\right) \\
&\text{s.t. } [\boldsymbol{R}_x]_{m,m} = 1, m = 1, 2, \cdots, M_T \\
&\qquad \|\boldsymbol{R}_x - \boldsymbol{I}_{M_T}\|^2 \leq \mu \qquad \boldsymbol{\Sigma}_x \succeq \mathbf{0},
\end{aligned}$$

with $\boldsymbol{\Sigma}_x = \boldsymbol{R}_x \otimes \boldsymbol{I}_{M_R}$. Notice that, since $\boldsymbol{\Pi} \succeq \boldsymbol{B}$ implies $\mathrm{Tr}\,(\boldsymbol{\Pi}) \geq \mathrm{Tr}\,(\boldsymbol{B})$, the problem

$$\max_{\boldsymbol{\Pi}} -\mathrm{Tr}(\boldsymbol{\Pi}) \quad \text{s.t. } \boldsymbol{\Pi} \succeq \boldsymbol{B}$$

admits $\mathrm{Tr}(\boldsymbol{\Pi}) = \mathrm{Tr}(\boldsymbol{B})$ as unique solution. Thus maximizing the objective function in (21) boils down to solving the problem

$$\begin{aligned}
&\max_{\boldsymbol{\Sigma}_x, \boldsymbol{\Pi}} \left[\mathrm{Tr}\left(\boldsymbol{E}^H \boldsymbol{\Sigma}_x \boldsymbol{E}\right) - \mathrm{Tr}\,(\boldsymbol{\Pi})\right] \\
&\boldsymbol{\Pi} \geq \boldsymbol{E}^H \boldsymbol{\Sigma}_x \boldsymbol{A}_0 (\boldsymbol{A}_0^H \boldsymbol{\Sigma}_x \boldsymbol{A}_0)^{-1} \boldsymbol{A}_0^H \boldsymbol{\Sigma}_x \boldsymbol{E}
\end{aligned}$$

The constraint is obviously satisfied since the Schur complement of the matrix

$$\boldsymbol{\Lambda} = \begin{bmatrix} \boldsymbol{\Pi} & \boldsymbol{E}^H (\boldsymbol{R}_x \otimes \boldsymbol{I}_{M_R}) \boldsymbol{A}_0 \\ \boldsymbol{A}_0^H (\boldsymbol{R}_x \otimes \boldsymbol{I}_{M_R}) \boldsymbol{E} & (\boldsymbol{A}_0^H (\boldsymbol{R}_x \otimes \boldsymbol{I}_{M_R}) \boldsymbol{A}_0) \end{bmatrix}$$

with respect to the block $(\boldsymbol{A}_0^H (\boldsymbol{R}_x \otimes \boldsymbol{I}_{M_R}) \boldsymbol{A}_0)$ is semi-definite positive, and the matrix $\boldsymbol{\Pi}$ is necessarily also positive semi-definite. As a consequence, waveform optimization reduces to solving the convex problem

$$\begin{aligned}
&\arg\max_{\boldsymbol{R}_x, \boldsymbol{\Pi}} \mathrm{Tr}\left(\boldsymbol{E}^H (\boldsymbol{R}_x \otimes \boldsymbol{I}_{M_R}) \boldsymbol{E} - \boldsymbol{\Pi}\right) \\
&\qquad \text{s.t. } [\boldsymbol{R}_x]_{m,m} = 1, m = 1, 2, \cdots, M_T \\
&\qquad\quad \boldsymbol{\Lambda} \succeq 0 \\
&\qquad\quad \|\boldsymbol{R}_x - \boldsymbol{I}_{M_T}\|^2 \leq \mu \\
&\qquad\quad \boldsymbol{R}_x \succeq \mathbf{0}.
\end{aligned} \tag{22}$$

Since (22) is a Semi-Definite Programming (SDP) problem, it can be solved efficiently by the convex optimization approach. Fig. 3 highlights the detector behavior for different values of $(K_0, K_1)$ and the impact of the number of system degrees of freedom $M_T M_R$. Not surprisingly, we observe that larger values of $K_1$ for fixed $K_0$ result in better detection performance. This is obviously because the two subspaces defined by the projection matrices $\boldsymbol{P}_0$ and $\boldsymbol{P}_1$ become more and more distinguishable as $K_1$ increases: the inevitable consequence is that the "worst case" is the situation where $K_0$ is large (in the plot, $K_0 = 3$) and $K_1$ small (in the plot, $K_1 = 1$). In this figure, two types of waveforms are compared including the orthogonal waveform with $\boldsymbol{R}_x = \boldsymbol{I}_{M_T}$, the optimized waveform with the perfect parameter information of direct and first-order paths. By optimizing the transmit waveform, a significant improvement in target detection performance can be achieved.

## IV. Angle estimation for multipaths

As anticipated, the test (13) is not implementable, in that the two matrices $\mathbf{A}(\boldsymbol{\Theta}_0)$ and $\mathbf{A}(\boldsymbol{\Theta}, \boldsymbol{\Phi})$ are not known even in their order. In principle, such a prior uncertainty could be addressed within the GLRT framework. Noticing that directly solving the problems $\min_{K_0, \boldsymbol{A}(\boldsymbol{\Theta}_0) \in \mathbb{C}^{M_T M_R \times K_0}} \| \boldsymbol{P}(\boldsymbol{\Theta}_0) \bar{\boldsymbol{z}} \|^2$ and $\min_{K_0, K_1, \boldsymbol{A}(\boldsymbol{\Theta}, \boldsymbol{\Phi}) \in \mathbb{C}^{M_T M_R \times (K_0 + 2K_1)}} \| \boldsymbol{P}(\boldsymbol{\Theta}, \boldsymbol{\Phi}) \bar{\boldsymbol{z}} \|^2$ leads to an overestimation of the model order. To address this, we introduce the sparsity of the reflection paths for estimating $\mathbf{A}(\boldsymbol{\Theta}_0)$ and $\mathbf{A}(\boldsymbol{\Theta}, \boldsymbol{\Phi})$. This sparsity can be justified by the fact that automotive radar systems, typically equipped with an array configuration of at least 3 transmitters and 4 receivers (i.e. $M_T M_R > 12$), utilize mm-wave technology with a wide

This article has been accepted for publication in IEEE Transactions on Signal Processing. This is the author's version which has not been fully edited and content may change prior to final publication. Citation information: DOI 10.1109/TSP.2024.3384750



bandwidth for high range resolution. As a result, only a limited number of targets, usually fewer than three, are present within the same delay-Doppler bin [6], meaning $K_0$ and $K_1$ are usually much smaller than $M_T M_R$ [43]. Specifically, we try to resolve the following problem assuming $\mathcal{H}_0$ hypothesis is true:

$$\begin{aligned}(\hat{K}_0, \widehat{\boldsymbol{\Theta}}_0, \hat{\boldsymbol{\alpha}}) = & \mathop{\arg\min}_{\boldsymbol{\Theta}_0 \in \mathbb{R}^{K_0\times 1}, \boldsymbol{\alpha}\in\mathbb{C}^{K_0\times 1}, K_0} K_0 \\ \text{s.t.} & \left\|\bar{\boldsymbol{z}} - \bar{\mathbf{A}}(\boldsymbol{\Theta}_0)\boldsymbol{\alpha}\right\|_2^2 \leq \epsilon^2,\end{aligned} \tag{23}$$

where $\bar{\mathbf{A}}(\cdot) = \boldsymbol{\Sigma}_x^{1/2}\mathbf{A}(\cdot)$, and obtain a suitable estimation of the direct paths $\widehat{\boldsymbol{\Theta}}_0$. It is worth noting that for any $\boldsymbol{\Theta}_0$, $\boldsymbol{\alpha}$ should be $\bar{\mathbf{A}}^\dagger(\boldsymbol{\Theta}_0)\bar{\boldsymbol{z}}$ to minimize $\left\|\bar{\boldsymbol{z}} - \bar{\mathbf{A}}(\boldsymbol{\Theta}_0)\boldsymbol{\alpha}\right\|^2$, so the constraints degrades to $\| \boldsymbol{P}(\boldsymbol{\Theta}_0)\bar{\boldsymbol{z}} \|_2^2 \leq \epsilon$.

Similarly, assuming $\mathcal{H}_1$ hypothesis is true, we resort to:

$$\begin{aligned}(\hat{K}_0, \hat{K}_1, \widehat{\boldsymbol{\Theta}}, \widehat{\boldsymbol{\Phi}}, \hat{\boldsymbol{\beta}}) = & \mathop{\arg\min}_{\substack{K_0, K_1, \\ \boldsymbol{\Theta}\in\mathbb{R}^{(K_0+2K_1)\times 1}, \\ \boldsymbol{\Phi}\in\mathbb{R}^{(K_0+2K_1)\times 1}, \\ \boldsymbol{\beta}\in\mathbb{C}^{(K_0+2K_1)\times 1}}} K_0 + \delta K_1 \\ \text{s.t.} & \left\|\bar{\boldsymbol{z}} - \bar{\mathbf{A}}(\boldsymbol{\Theta}, \boldsymbol{\Phi})\boldsymbol{\beta}\right\|_2^2 \leq \epsilon^2,\end{aligned} \tag{24}$$

where $\delta$ is the parameter characterizing the weights between $K_0$ and $K_1$. The test family is then applied for the detection of $\mathcal{H}_1$ from $\mathcal{H}_0$

$$\frac{\| (\boldsymbol{I}_{M_T M_R} - \bar{\mathbf{A}}(\widehat{\boldsymbol{\Theta}}_0)\bar{\mathbf{A}}^\dagger(\widehat{\boldsymbol{\Theta}}_0)\bar{\boldsymbol{z}} \|^2}{\| (\boldsymbol{I}_{M_T M_R} - \bar{\mathbf{A}}(\widehat{\boldsymbol{\Theta}}, \widehat{\boldsymbol{\Phi}})\bar{\mathbf{A}}^\dagger(\widehat{\boldsymbol{\Theta}}, \widehat{\boldsymbol{\Phi}})\bar{\boldsymbol{z}} \|^2} \underset{\mathcal{H}_0}{\overset{\mathcal{H}_1}{\gtrless}} \lambda_G. \tag{25}$$

The next two subsections are thus devoted to illustrating how the needed estimators may be designed to solve (23) and (24) through bounded-complexity procedures.

### A. Estimators for $\boldsymbol{\Theta}_0$ under $\mathcal{H}_0$ hypothesis

We propose here an iterative procedure to solve (23). We define $\boldsymbol{r}^{(t)}$ as the residual in the $t$-th iteration, obtained by subtracting the contribution from the estimated angles at that iteration. It is initialized as $\mathbf{r}^{(0)} = \bar{\boldsymbol{z}}$. As to the set of the angles of the direct paths, it is initialized as the empty set, i.e. $\widehat{\boldsymbol{\Theta}}_0^{(0)} = \emptyset$ and $\hat{K}_0^{(0)} = 0$. The algorithm thus entails an initial search over a uniform grid of size $G$, $\{\tilde{\theta}_1, \tilde{\theta}_2, \ldots, \tilde{\theta}_G\}$ say, and successive refinement of the estimate in a continuous domain.

In the $t$-th iteration, we insert a path into the set and $\hat{K}_0^{(t)}$ is updated as $\hat{K}_0^{(t)} = \hat{K}_0^{(t-1)} + 1$. The minimization of the $\ell_2$-norm of the residual entails evaluating

$$\hat{\theta}^{(t)} = \mathop{\arg\max}_{\theta^{(t)}\in\{\tilde{\theta}_1, \tilde{\theta}_2, \cdots, \tilde{\theta}_G\}} |(\mathbf{r}^{(t-1)})^H \mathbf{a}(\theta^{(t)})|, \tag{26}$$

and updating the angle matrix as $\widehat{\boldsymbol{\Theta}}_0^{(t,0)} = [(\widehat{\boldsymbol{\Theta}}_0^{(t-1)})^T, \hat{\theta}^{(t)}]^T$. The accuracy of this estimate is subsequently enhanced by using Gauss–Newton (GN) iterations adopting the results of the on-grid search, i.e. $\widehat{\boldsymbol{\Theta}}_0^{(t,0)}$, as the initial point. The GN method thus updates such an estimate through the inner iteration

$$\widehat{\boldsymbol{\Theta}}_0^{(t,i+1)} = \widehat{\boldsymbol{\Theta}}_0^{(t,i)} - (\mathbf{H}_0^{(t,i)})^{-1}\mathbf{g}_0^{(t,i)}, \tag{27}$$

where $\mathbf{g}_0^{(t,i)}$ and $\mathbf{H}_0^{(t,i)}$ denoting gradient and Hessian of the function $F(\boldsymbol{\Theta}_0^{(t,i)}) = \| \bar{\boldsymbol{z}} - \bar{\mathbf{A}}(\boldsymbol{\Theta}_0^{(t,i)})\bar{\mathbf{A}}^\dagger(\boldsymbol{\Theta}_0^{(t,i)})\bar{\boldsymbol{z}} \|_2^2$, respectively. Define $\bar{\mathbf{A}}_0^{(t,i)} = \bar{\mathbf{A}}(\boldsymbol{\Theta}_0^{(t,i)})$, $\boldsymbol{P}_0^{(t,i)} = \boldsymbol{P}(\boldsymbol{\Theta}_0^{(t,i)})$. Following the derivations in Appendix A, the expressions of $\mathbf{H}_0^{(t,i)}$ and $\mathbf{g}_0^{(t,i)}$ are given by

$$\mathbf{g}_0^{(t,i)} = -2\mathrm{Re}\left\{\mathrm{diag}\{(\bar{\mathbf{A}}_0^{(t,i)})^\dagger \bar{\boldsymbol{z}}\bar{\boldsymbol{z}}^H \boldsymbol{P}_0^{(t,i)}\mathbf{D}_0^{(t,i)}\}\right\}, \tag{28}$$

$$\begin{aligned}\mathbf{H}_0^{(t,i)} = & 2\mathrm{Re}\left\{(\mathbf{D}_0^{(t,i)})^H \boldsymbol{P}_0^{(t,i)}\mathbf{D}_0^{(t,i)} \right. \\ & \left. \odot \left((\mathbf{A}_0^{(t,i)})^\dagger \bar{\boldsymbol{z}}\bar{\boldsymbol{z}}^H((\mathbf{A}_0^{(t,i)})^\dagger)^H\right)^T\right\} \\ & + 2\mathrm{Re}\left\{(\mathbf{D}_0^{(t,i)})^H \boldsymbol{P}_0^{(t,i)}\bar{\boldsymbol{z}}\bar{\boldsymbol{z}}^H \boldsymbol{P}_0^{(t,i)}(\mathbf{D}_0^{(t,i)})^T \right. \\ & \left. \odot \left((\bar{\mathbf{A}}_0^{(t,i)})^\dagger((\bar{\mathbf{A}}_0^{(t,i)})^\dagger)^H\right)\right\}\end{aligned}, \tag{29}$$

where $\mathbf{D}_0^{(t,i)} = \left[\frac{\partial\bar{\mathbf{a}}(\hat{\theta}_1^{(i)})}{\partial\hat{\theta}_1^{(i)}}, \frac{\partial\bar{\mathbf{a}}(\hat{\theta}_2^{(i)})}{\partial\hat{\theta}_2^{(i)}}, \ldots, \frac{\partial\bar{\mathbf{a}}(\hat{\theta}_t^{(i)})}{\partial\bar{\mathbf{a}}\hat{\theta}_t^{(i)}}\right]^T$ with $\bar{\mathbf{a}}(\hat{\theta}_j^{(i)}) = \boldsymbol{\Sigma}_x^{1/2}\mathbf{a}(\hat{\theta}_j^{(i)})$ for $j = 1, 2, \ldots, t$.

The above computations are carried out iteratively until a maximum iteration number $I$ is reached, whereby $\widehat{\boldsymbol{\Theta}}_0^{(t,I)}$ is adopted as the refined estimated angle $\widehat{\boldsymbol{\Theta}}_0^{(t)}$ in the $t$-th iteration. This allows updating the amplitude estimates and the residual as:

$$\hat{\boldsymbol{\alpha}}^{(t)} = \bar{\mathbf{A}}^\dagger(\widehat{\boldsymbol{\Theta}}_0^{(t)})\bar{\boldsymbol{z}}, \tag{30}$$

$$\mathbf{r}^{(t)} = \bar{\boldsymbol{z}} - \bar{\mathbf{A}}(\widehat{\boldsymbol{\Theta}}_0^{(t)})\hat{\boldsymbol{\alpha}}^{(t)}. \tag{31}$$

In principle, the iterative process stops when $\|\mathbf{r}^{(t)}\|_2 \leq \epsilon$ i.e the condition of (23) is satisfied. Additionally, considering the potential issue of overestimating $K_0$, we also set a maximum number of iterations $T$. The iterative process will be terminated if $t \geq T$ or $\|\mathbf{r}^{(t-1)}\|_2 - \|\mathbf{r}^{(t)}\|_2 \leq \epsilon_1$. The detailed procedure is given in Algorithm 1 and we name the proposed method as Compressed Sensing method in Continuous Domain under hypothesis $\mathcal{H}_0$ (CSCD-H0) algorithm.

It is worth noticing that, without the refinement step, the algorithm would reduce to an Orthogonal Matching Pursuit (OMP) algorithm [44], which is a classic method in CS. As OMP does not involve grid refinement in the continuous domain, a simplification may cause a remarkable performance impairment due to the well-known off-grid problem and would likely lead to overestimating the value of $K_0$.

### B. Estimators for $(\boldsymbol{\Theta}, \boldsymbol{\Phi})$ under $\mathcal{H}_1$ hypothesis

Under $\mathcal{H}_1$, the algorithm we propose is an extension of the previous one, on the understanding that now the angles of both direct and first-order paths must be estimated. To reduce interference between direct and first-order paths, we implement the estimation procedures separately on direct and first-order paths and subsequently decide the estimated paths that should be retained. The initial values of the relevant parameters are of course $\mathbf{r}^{(0)} = \mathbf{z}, \widehat{\boldsymbol{\Theta}}_1^{(0)} = \emptyset, \widehat{\boldsymbol{\Phi}}_1^{(0)} = \emptyset, \widehat{\boldsymbol{\Theta}}_0^{(0)} = \emptyset$, $\hat{K}_1^{(0)} = 0$, $\hat{K}_0^{(0)} = 0$.

Assume we want to estimate an additional direct path. Again, we first undertake a search on a $G-$dimensional grid of the common values of its DOA and DOD according to (26), thus obtaining a coarse estimate of the angle set $\bar{\boldsymbol{\Theta}}^{(t,0)} =$

**Algorithm 1:** CSCD-H0 algorithm

```
Input: $\bar{z}$, $\{\tilde{\theta}_1, \tilde{\theta}_2, \ldots, \tilde{\theta}_G\}$ and $T$, $I$, $\epsilon$, $\epsilon_1$;
Output: $\hat{K}_0$, $\hat{\boldsymbol{\alpha}} \in \mathbb{C}^{\hat{K}_0 \times 1}$, $\widehat{\boldsymbol{\Theta}}_0 \in \mathbb{R}^{\hat{K}_0 \times 1}$;
Initialization: $\widehat{\boldsymbol{\Theta}}_0^{(0)} = \emptyset$ and $\hat{K}_0^{(0)} = 0, \mathbf{r}^{(0)} = \bar{z}, t = 0$;
while $\|\mathbf{r}^{(t)}\|_2 > \epsilon$ do
    $t \leftarrow t + 1$;
    Obtain the inserted angle $\hat{\theta}^{(t)}$ via (26);
    $\widehat{\boldsymbol{\Theta}}_0^{(t,0)} = [(\widehat{\boldsymbol{\Theta}}_0^{(t-1)})^T, \hat{\theta}^{(t)}]^T$, $\hat{K}_0^{(t)} = \hat{K}_0^{(t-1)} + 1$;
    for $i = 0$ to $I$ do
        Calculate $\mathbf{g}_0^{(t,i)}$ and $\mathbf{H}_0^{(t,i)}$ according to (28)
          and (29), respectively;
        Update $\widehat{\boldsymbol{\Theta}}_0^{(t,i+1)}$ by (27);
    end
    Update $\widehat{\boldsymbol{\Theta}}_0^{(t)} \leftarrow \widehat{\boldsymbol{\Theta}}_0^{(t,I)}$,
    Update $\hat{\boldsymbol{\alpha}}^{(t)}$ and residue $\mathbf{r}^{(t)}$ by (30) and (31),
      respectively;
    if $t \geq T$ or $\|\mathbf{r}^{(t-1)}\|_2 - \|\mathbf{r}^{(t)}\|_2 \leq \epsilon_1$ then
        Break;
    end
end
Return: $\widehat{\boldsymbol{\Theta}}_0 = \widehat{\boldsymbol{\Theta}}_0^{(t)}$, $\hat{\boldsymbol{\alpha}} = \hat{\boldsymbol{\alpha}}^{(t)}$, $\hat{K}_0 = \hat{K}_0^{(t)}$ .
```

$[\bar{\boldsymbol{\Theta}}_1^{(t,0)}; \bar{\boldsymbol{\Phi}}_1^{(t,0)}; \bar{\boldsymbol{\Theta}}_0^{(t,0)}]$ with $\bar{\boldsymbol{\Theta}}_1^{(t,0)} = \widehat{\boldsymbol{\Theta}}_1^{(t-1)}, \bar{\boldsymbol{\Phi}}_1^{(t,0)} = \widehat{\boldsymbol{\Phi}}_1^{(t-1)}$ and $\bar{\boldsymbol{\Theta}}_0^{(t,0)} = [(\widehat{\boldsymbol{\Theta}}_0^{(t-1)})^T, \hat{\theta}^{(t)}]^T$.

In order to search for an additional first-order path pair, coarse estimates of the angle pair $(\hat{\vartheta}^{(t)}, \hat{\varphi}^{(t)})$ are again obtained via search on two uniform $G$-dimensional grids $\boldsymbol{\Xi}_t = \{\tilde{\vartheta}_1, \tilde{\vartheta}_2, \ldots, \tilde{\vartheta}_G\}$ and $\boldsymbol{\Xi}_r = \{\tilde{\varphi}_1, \tilde{\varphi}_2, \ldots, \tilde{\varphi}_G\}$:

$$(\hat{\vartheta}^{(t)}, \hat{\varphi}^{(t)}) = \underset{\substack{\vartheta^{(t)} \in \boldsymbol{\Xi}_t \\ \varphi^{(t)} \in \boldsymbol{\Xi}_r \\ \vartheta^{(t)} < \varphi^{(t)}}}{\arg\max} \Big( |(\mathbf{r}^{(t-1)})^H (\mathbf{a}_T(\vartheta^{(t)}) \circ \mathbf{a}_R(\varphi^{(t)}))| + |(\mathbf{r}^{(t-1)})^H (\mathbf{a}_T(\varphi^{(t)}) \circ \mathbf{a}_R(\vartheta^{(t)}))| \Big). \tag{32}$$

We thus have a coarse estimate of the angle set $\bar{\bar{\boldsymbol{\Theta}}}^{(t,0)} = [\bar{\bar{\boldsymbol{\Theta}}}_1^{(t,0)}; \bar{\bar{\boldsymbol{\Phi}}}_1^{(t,0)}; \bar{\bar{\boldsymbol{\Theta}}}_0^{(t,0)}]$ with $\bar{\bar{\boldsymbol{\Theta}}}_1^{(t,0)} = [(\widehat{\boldsymbol{\Theta}}_1^{(t-1)})^T, \hat{\vartheta}^{(t)}]^T, \bar{\bar{\boldsymbol{\Phi}}}_1^{(t,0)} = [(\widehat{\boldsymbol{\Phi}}_1^{(t-1)})^T, \hat{\varphi}^{(t)}]^T$ and $\bar{\bar{\boldsymbol{\Theta}}}_0^{(t,0)} = \widehat{\boldsymbol{\Theta}}_0^{(t-1)}$. The refinement steps of the two estimates above via search on a continuous domain have the same rationale as for the case illustrated in the previous subsection. Due to the mixture of direct and first-order paths under the $\mathcal{H}_1$ hypothesis, the GN method may lead to unstable estimation due to the rank-deficiency in Hessian when the difference between DOD and DOA is not large [2]. Therefore, we resort to the LM method [45] for updating angle estimates.

For brevity, here we outline the LM iteration for the search of an additional direct path since the search for an additional first-order path follows the same flow with $\bar{\boldsymbol{\Theta}}^{(t,0)}$ replaced by $\bar{\bar{\boldsymbol{\Theta}}}^{(t,0)}$. The angle set is updated as $\bar{\boldsymbol{\Theta}}^{(t,i+1)} = \bar{\boldsymbol{\Theta}}^{(t,i)} + \mathbf{h}^{(t,i)}$, where

$$\mathbf{h}^{(t,i)} = -(\mathbf{H}^{(t,i)} + \mu^{(t,i)} \boldsymbol{I}_{\hat{K}^{(t)}})^{-1} \mathbf{g}^{(t,i)}, \tag{33}$$

[2]An example will be given to illustrate this problem

with $\mathbf{H}^{(t,i)}$ and $\mathbf{g}^{(t,i)}$ denoting the Hessian and gradient of $\bar{F}(\bar{\boldsymbol{\Theta}}^{(t,i)}) = \| \bar{\boldsymbol{z}} - \mathbf{A}(\bar{\boldsymbol{\Theta}}^{(t,i)}, \bar{\boldsymbol{\Phi}}^{(t,i)}) \mathbf{A}^{\dagger}(\bar{\boldsymbol{\Theta}}^{(t,i)}, \bar{\boldsymbol{\Phi}}^{(t,i)}) \bar{\boldsymbol{z}} \|_2^2$, respectively. $\hat{K}^{(t)}$ denotes the size of $\bar{\boldsymbol{\Theta}}^{(t,i)}$, $\mu^{(t,i)}$ is a damping parameter. We emphasize that the quantities $\mathbf{g}^{(t,i)}$ and $\mathbf{H}^{(t,i)}$ are different from those under $\mathcal{H}_0$ . In fact, $\mathbf{g}^{(t,i)}$ should now be partitioned as:

$$\mathbf{g}^{(t,i)} = \left[ \mathbf{g}_{\mathrm{T}}^{(t,i)}; \mathbf{g}_{\mathrm{R}}^{(t,i)}; {\mathbf{g}'_0}^{(t,i)} \right], \tag{34}$$

where $\mathbf{g}_{\mathrm{T}}^{(t,i)}$ and $\mathbf{g}_{\mathrm{R}}^{(t,i)}$ denote the gradients of $\bar{F}$ with respect to DOD's and DOA's of first-order paths, respectively, while ${\mathbf{g}'_0}^{(t,i)}$ denotes the gradient of $\bar{F}$ with respect to the DOA's of direct paths: closed-form expressions of these quantities are given in (44) -(46) of Appendix B. Similarly, the matrix $\mathbf{H}^{(t,i)}$ is written as

$$\mathbf{H}^{(t,i)} = \begin{bmatrix} \mathbf{H}_{\mathrm{TT}}^{(t,i)} & \mathbf{H}_{\mathrm{TR}}^{(t,i)} & \mathbf{H}_{\mathrm{T0}}^{(t,i)} \\ \mathbf{H}_{\mathrm{RT}}^{(t,i)} & \mathbf{H}_{\mathrm{RR}}^{(t,i)} & \mathbf{H}_{\mathrm{R0}}^{(t,i)} \\ \mathbf{H}_{\mathrm{0T}}^{(t,i)} & \mathbf{H}_{\mathrm{0R}}^{(t,i)} & \mathbf{H}_{00}^{(t,i)} \end{bmatrix}, \tag{35}$$

and explicit forms for the different blocks are given in (50)-(58) of Appendix B.

We explicitly note here that paths with unequal DOD and DOA are added in pairs by (32), namely, first-order paths always appear in a paired, group-sparse manner. This group-sparse characteristic is rare in the interference from direct paths or grating lobes caused by sparse linear array (SLA). When calculating derivatives in $\mathbf{g}^{(t,i)}$ and $\mathbf{H}^{(t,i)}$, the pairwise constraint of the first-order paths must be considered. For instance, when calculating the derivative of $\bar{F}$ with respect to $\hat{\vartheta}^{(t)}$, the derivative of both $\mathbf{a}_T(\hat{\vartheta}^{(t)}) \circ \mathbf{a}_R(\hat{\varphi}^{(t)})$ and $\mathbf{a}_T(\hat{\varphi}^{(t)}) \circ \mathbf{a}_R(\hat{\vartheta}^{(t)})$ should be calculated. This allows the algorithm to leverage the group-sparsity of the first-order paths to enhance the estimation accuracy.

The damping parameter $\mu^{(t,i)}$ in (33) is selected by a line search algorithm that is controlled by the gain ratio

$$\varrho^{(t,i)} = \frac{\bar{F}(\bar{\boldsymbol{\Theta}}^{(t,i)}) - \bar{F}(\bar{\boldsymbol{\Theta}}^{(t,i)} + \mathbf{h}^{(t,i)})}{\frac{1}{2}(\mathbf{h}^{(t,i)})^H (\mu^{(t,i)} \mathbf{h}^{(t,i)} - \mathbf{g}^{(t,i)})}. \tag{36}$$

Steps 9-14 in Algorithm 2 describe how this parameter is obtained.

Once the refinement step is over, we obtain the angle set $\bar{\boldsymbol{\Theta}}^{(t,T)} = [\bar{\boldsymbol{\Theta}}_1^{(t,I)}; \bar{\boldsymbol{\Phi}}_1^{(t,I)}; \bar{\boldsymbol{\Theta}}_0^{(t,I)}]$ and the residual $\boldsymbol{r}_1^{(t)}$ for the estimate of an additional direct path, and $\bar{\bar{\boldsymbol{\Theta}}}^{(t,T)} = [\bar{\bar{\boldsymbol{\Theta}}}_1^{(t,I)}; \bar{\bar{\boldsymbol{\Phi}}}_1^{(t,I)}; \bar{\bar{\boldsymbol{\Theta}}}_0^{(t,I)}]$ and $\boldsymbol{r}_2^{(t)}$ for the estimate of an additional pair of first-order paths. A decision on which model better fits the observation is thus made based on the quantity $r^{(t)} = \|\boldsymbol{r}_2^{(t)}\|_2 - \|\boldsymbol{r}_1^{(t)}\|_2$ through

$$(\widehat{\boldsymbol{\Theta}}_1^{(t)}, \widehat{\boldsymbol{\Phi}}_1^{(t)}, \widehat{\boldsymbol{\Theta}}_0^{(t)}) = \begin{cases} (\bar{\boldsymbol{\Theta}}_1^{(t,I)}, \bar{\boldsymbol{\Phi}}_1^{(t,I)}, \bar{\boldsymbol{\Theta}}_0^{(t,I)}) & r^{(t)} > \delta_r \\ (\bar{\bar{\boldsymbol{\Theta}}}_1^{(t,I)}, \bar{\bar{\boldsymbol{\Phi}}}_1^{(t,I)}, \bar{\bar{\boldsymbol{\Theta}}}_0^{(t,I)}) & r^{(t)} < \delta_r \end{cases}$$

where $\delta_r$ is a suitably set threshold.

The proposed algorithm, named Compressed Sensing method in Continuous Domain under hypothesis $\mathcal{H}_1$ (CSCD-H1), is summarized in Algorithm 2 and, like CSCD-H0, reduces to a kind of Group OMP (GOMP) as the refinement phase is omitted.

We illustrate the convergence of the GN and LM methods implementation of the refined estimation through a simulation

This article has been accepted for publication in IEEE Transactions on Signal Processing. This is the author's version which has not been fully edited and content may change prior to final publication. Citation information: DOI 10.1109/TSP.2024.3384750



**Algorithm 2:** CSCD-H1 algorithm

**Input:** $\bar{z}$, $\Xi_t$, $\Xi_r$ and $T$, $I$, $J$,$\epsilon$,$\epsilon_2$, $\delta_r$ ;

**Output:** $\hat{K}_1$, $\hat{K}_0$, $\widehat{\mathbf{\Theta}}$, $\widehat{\mathbf{\Phi}}$, $\hat{\boldsymbol{\beta}}$;

1 **Initialization:** $\widehat{\mathbf{\Theta}}_1^{(0)} = \emptyset$, $\widehat{\mathbf{\Phi}}_1^{(0)} = \emptyset$, $\widehat{\mathbf{\Theta}}_0^{(0)} = \emptyset$, $\mathbf{r}^{(0)} = \bar{z}$, $t = 0$;

2 **while** $\|\mathbf{r}^{(t)}\|_2 > \epsilon$ **do**

3 $t \leftarrow t + 1$;

4 Obtain the angle of direct path $\hat{\theta}^{(t)}$ via (26);

5 Obtain $\bar{\mathbf{\Theta}}^{(t,0)} = [\bar{\mathbf{\Theta}}_1^{(t,0)}; \bar{\mathbf{\Phi}}_1^{(t,0)}; \bar{\mathbf{\Theta}}_0^{(t,0)}]$ where $\bar{\mathbf{\Theta}}_1^{(t,0)} = \widehat{\mathbf{\Theta}}_1^{(t-1)}$, $\bar{\mathbf{\Phi}}_1^{(t,0)} = \widehat{\mathbf{\Phi}}_1^{(t-1)}$ and $\bar{\mathbf{\Theta}}_0^{(t,0)} = [(\widehat{\mathbf{\Theta}}_0^{(t-1)})^T, \hat{\theta}^{(t)}]^T$;

6 **for** $i = 0$ *to* $I$ **do**

7 Calculate $\mathbf{g}^{(t,i)}$ and $\mathbf{H}^{(t,i)}$ using (34) and (35), respectively;

8 Calculate $\mathbf{h}^{(t,i)}$ and $\varrho^{(t,i)}$ by (33) and (36), respectively;

9 $j \leftarrow 0$;

10 **while** $\varrho^{(t,i)} \leq 0$ and $j < J$ **do**

11 Update $j \leftarrow j + 1$, $\mu^{(t,i)} \leftarrow 2^j \mu^{(t,i)}$;

12 Calculate $\mathbf{h}^{(t,i)}$ and $\varrho^{(t,i)}$ by (33) and (36), respectively;

13 **end**

14 $\mu^{(t,i+1)} = \mu^{(t,i)} \max\{\frac{1}{3}, 1 - (2\varrho^{(t,i)} - 1)^3\}$;

15 $\bar{\mathbf{\Theta}}^{(t,i+1)} = \bar{\mathbf{\Theta}}^{(t,i)} + \mathbf{h}^{(t,i)}$;

16 **end**

17 $\boldsymbol{r}_1^{(t)} = \bar{z} - \bar{\mathbf{A}}(\bar{\mathbf{\Theta}}^{(t,I)}, \bar{\mathbf{\Phi}}^{(t,I)})\bar{\mathbf{A}}^\dagger(\bar{\mathbf{\Theta}}^{(t,I)}, \bar{\mathbf{\Phi}}^{(t,I)})\bar{z}$;

18 Obtain the inserted angle pair $(\hat{\vartheta}^{(t)}, \hat{\varphi}^{(t)})$ via (32);

19 Obtain $\bar{\bar{\mathbf{\Theta}}}^{(t,0)} = [\bar{\bar{\mathbf{\Theta}}}_1^{(t,0)}; \bar{\bar{\mathbf{\Phi}}}_1^{(t,0)}; \bar{\bar{\mathbf{\Theta}}}_0^{(t,0)}]$ where $\bar{\bar{\mathbf{\Theta}}}_1^{(t,0)} = [(\widehat{\mathbf{\Theta}}_1^{(t-1)})^T, \hat{\vartheta}^{(t)}]^T$, $\bar{\bar{\mathbf{\Phi}}}_1^{(t,0)} = [(\widehat{\mathbf{\Phi}}_1^{(t-1)})^T, \hat{\varphi}^{(t)}]^T$ and $\bar{\bar{\mathbf{\Theta}}}_0^{(t,0)} = \widehat{\mathbf{\Theta}}_0^{(t-1)}$;

20 Optimize the $\bar{\bar{\mathbf{\Theta}}}^{(t,0)}$ based on the LM method given by step 6 to step 16 with $\bar{\mathbf{\Theta}}^{(t,0)}$ replaced by $\bar{\bar{\mathbf{\Theta}}}^{(t,0)}$;

21 $\boldsymbol{r}_2^{(t)} = \bar{z} - \bar{\mathbf{A}}(\bar{\bar{\mathbf{\Theta}}}^{(t,I)}, \bar{\bar{\mathbf{\Phi}}}^{(t,I)})\bar{\mathbf{A}}^\dagger(\bar{\bar{\mathbf{\Phi}}}^{(t,I)}, \bar{\bar{\mathbf{\Theta}}}^{(t,I)})\bar{z}$;

22 Calculate $r^{(t)} = \|\boldsymbol{r}_2^{(t)}\|_2 - \|\boldsymbol{r}_1^{(t)}\|_2$;

23 **if** $r^{(t)} < \delta_r$ **then**

24 $(\widehat{\mathbf{\Theta}}_1^{(t)}, \widehat{\mathbf{\Phi}}_1^{(t)}, \widehat{\mathbf{\Theta}}_0^{(t)}) = (\bar{\mathbf{\Theta}}_1^{(t,I)}, \bar{\mathbf{\Phi}}_1^{(t,I)}, \bar{\mathbf{\Theta}}_0^{(t,I)})$;

25 $\boldsymbol{r}^{(t)} = \boldsymbol{r}_2^{(t)}$.

26 **else**

27 $(\widehat{\mathbf{\Theta}}_1^{(t)}, \widehat{\mathbf{\Phi}}_1^{(t)}, \widehat{\mathbf{\Theta}}_0^{(t)}) = (\bar{\bar{\mathbf{\Theta}}}_1^{(t,I)}, \bar{\bar{\mathbf{\Phi}}}_1^{(t,I)}, \bar{\bar{\mathbf{\Theta}}}_0^{(t,I)})$;

28 $\boldsymbol{r}^{(t)} = \boldsymbol{r}_1^{(t)}$.

29 **end**

30 **if** $t \geq T$ or $\|\mathbf{r}^{(t-1)}\|_2 - \|\mathbf{r}^{(t)}\|_2 \leq \epsilon_2$ **then**

31 Break;

32 **end**

33 **end**

34 Return: $\widehat{\mathbf{\Theta}} = [\widehat{\mathbf{\Theta}}_1^{(t)}, \widehat{\mathbf{\Phi}}_1^{(t)}, \widehat{\mathbf{\Theta}}_0^{(t)}]$, $\widehat{\mathbf{\Phi}} = [\widehat{\mathbf{\Phi}}_1^{(t)}, \widehat{\mathbf{\Theta}}_1^{(t)}, \widehat{\mathbf{\Theta}}_0^{(t)}]$, $\hat{\boldsymbol{\beta}} = \bar{\mathbf{A}}^\dagger(\widehat{\mathbf{\Theta}}, \widehat{\mathbf{\Phi}})\bar{z}$, length of $\widehat{\mathbf{\Theta}}_1^{(t)}$ as $\hat{K}_1$, length of $\widehat{\mathbf{\Theta}}_0^{(t)}$ as $\hat{K}_0$

example. In Fig. 4, we compared the curves of the loss function $F$ with the number of iterations during the optimization processes using both GN and LM methods. Specifically, Fig. 4a demonstrates similar convergence behavior for both methods in the scenarios with a large difference between DOD and DOA angles. However, when small differences between DOD and DOA angles are present, as shown in Fig. 4b, the GN method faces challenges in achieving convergence. The instability of the GN method can be attributed to the rank-deficiency in the Hessian matrix. Conversely, the LM method incorporates a regularization term to address this problem and demonstrates more robustness in these scenarios.

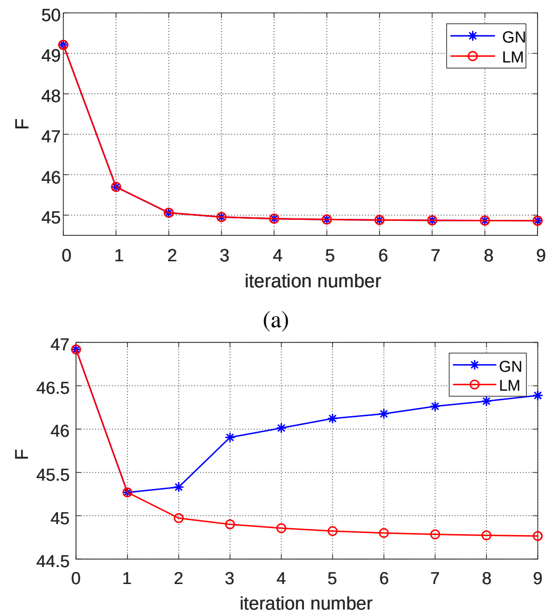


Fig. 4: Plots of cost function against the iteration number: (a) First-order path with $(-1.9°, -13.2°)$, (b) First-order path with $(-1.9°, -3.2°)$.

## V. Simulation and Experimental Results

### A. Simulation setup

In this section, numerical simulations are conducted to evaluate the performance of the proposed algorithm. For the proposed detection scheme, CSCD-H0 is adopted under $\mathcal{H}_0$, and CSCD-H1 is adopted under $\mathcal{H}_1$, so the detector is named GLRT-CSCD for simplicity. Likewise, we have GLRT-OMP algorithms for the detectors with OMP-based estimators. We include the IAA-based and the least absolute shrinkage and selection operator (LASSO)-based methods in the GLRT test, denoting them as GLRT-IAA and GLRT-LASSO, respectively.

Note that the angle estimation is crucial for the detection performance, we compare the accuracy of different methods. We conduct comparisons between the OMP, IAA [46], and LASSO [47] methods against our proposed CSCD-H0 algorithm in $\mathcal{H}_0$ scenario. Similarly, we evaluate the performance of the GOMP, multipath IAA (MPIAA) [28], and group LASSO (GLASSO) [48] methods against our proposed CSCD-H1 algorithm in $\mathcal{H}_1$ scenario. With the estimated angle, GLRT is applied to detect whether the first-order indirect path exists.

Other simulation parameters are set as follows:

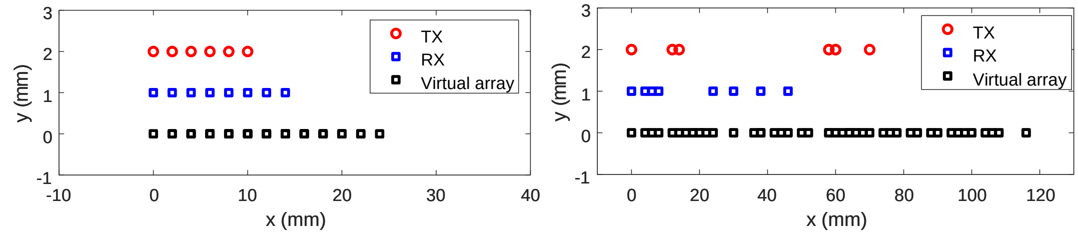


(a) (b)

Fig. 5: Real and virtual layouts of the MIMO radar antennas, (a) ULA, (b) SLA.

1) The radar operates at 79 GHz with carrier wavelength $\lambda = 3.8$mm. The number of transmitting elements $M_T = 6$ and receive element $M_R = 8$. We first conduct simulations with a uniform linear array (ULA) as illustrated in Fig. 5a. Moreover, by maintaining constant values for $M_T$ and $M_R$, we ensure a consistent upper bound in detection performance and subsequently verify the performance of an SLA as shown in Fig. 5b.
2) The noise is randomly generated according to a Gaussian distribution with the variance $\sigma^2 = 1$. The path amplitudes are generated according to $\boldsymbol{\beta} \sim \mathcal{CN}(0, \sigma_\beta^2 \boldsymbol{I}_{2K_1})$, $\boldsymbol{\alpha} \sim \mathcal{CN}(0, \sigma_\alpha^2 \boldsymbol{I}_{K_0})$. The signal-to-noise-ratio (SNR) of direct paths and first-order paths are defined as $\sigma_\alpha^2/\sigma^2$ and $\sigma_\beta^2/\sigma^2$, respectively.
3) The grids are obtained by discretizing angle space $[-90°, 90°]$ with a step of $2°$. The max iteration of the OMP, GOMP, CSCD-H0 and CSCD -H1 estimator are set to $T = 10$. The stop criterion parameters are set as $I = 10, \epsilon = \sqrt{\sigma^2 M_T M_R}$, $\epsilon_1 = 0.4$ and $\epsilon_2 = 0$. For CSCD-H1, we set parameters $\delta_r = \sigma$ and $J = 3$. The iteration number of IAA in $\mathcal{H}_0$ and $\mathcal{H}_1$ hypothesis are both set to 5, the regularization parameter of LASSO estimators are set as $2\sigma\sqrt{2\log G}$ in $\mathcal{H}_0$ and $2\sigma\sqrt{2\log(G^2)}$ in $\mathcal{H}_1$, respectively.
4) We evaluate the root-mean-squared-error (RMSE) of the angle estimation for the proposed algorithms. Notice that the algorithms return a bunch of estimations, corresponding to either true paths or erroneous ones, and the paths cannot be detected if there is no estimation close to its direction. We thus refer to the RMSEs conditioned on the correct path estimation. In undertaking simulations, a path is declared to be correctly estimated if its estimation error is smaller than the array beamwidth. Specifically, the RMSEs of the first-order path and direct path are calculated by

$$\mathrm{RMSE}_1 = \sqrt{\begin{array}{l} \frac{1}{\mathrm{MC}} \sum\limits_{m=1}^{\mathrm{MC}} \frac{1}{2|\boldsymbol{\Omega}_1^m|} \\ \cdot \sum\limits_{j \in \boldsymbol{\Omega}_1^m} \left( \begin{array}{c} (\vartheta_j^{(m)} - \hat{\vartheta}_j^{(m)})^2 \\ + (\varphi_j^{(m)} - \hat{\varphi}_j^{(m)})^2 \end{array} \right) \end{array}}, \quad (37)$$

$$\mathrm{RMSE}_0 = \sqrt{\frac{1}{\mathrm{MC}} \sum_{m=1}^{\mathrm{MC}} \frac{1}{|\boldsymbol{\Omega}_0^m|} \sum_{j \in \boldsymbol{\Omega}_0^m} (\theta_j^{(m)} - \hat{\theta}_j^{(m)})^2}, \quad (38)$$

respectively, where MC is the number of runs, $\boldsymbol{\Omega}_1^m$ and $\boldsymbol{\Omega}_0^m$ are the index set of the identified first-order paths and direct path in the $m$-th simulation respectively; $|\cdot|$ denotes the cardinality of the input set; $\vartheta_j^{(m)}$, $\varphi_j^{(m)}$ are the DOD and DOA the $j$-th first-order path in the $m$-th run and $\theta_j^{(m)}$ is the DOA of $j$-th direct path, while $\hat{\vartheta}_j^{(m)}$, $\hat{\varphi}_j^{(m)}$ and $\hat{\theta}_j^{(m)}$ are the estimates, respectively.
5) The detection performance of the proposed GLRT detector is compared with the performance bound derived in Sec. III-B. Specifically, the upper bound of $P_d$ is calculated by (20) under perfect angle estimation.
6) Unless specifically stated, the probability of false alarm is set to be $10^{-3}$, and the numbers of independent trials used for simulating the probabilities of false alarm and detection are $100/P_{fa}$ and $10^4$, respectively.

TABLE I: Complexity analysis

| Scenario | method | computational complexity |
|---|---|---|
| $\mathcal{H}_0$ | CSCD-H0 | $\mathcal{O}(GM_TM_RK_0 + K_0^2(M_TM_R)^2I)$ |
| | OMP | $\mathcal{O}(GM_TM_RK_0)$ |
| | IAA | $\mathcal{O}((G^2M_TM_R + M_TM_R^3)J)$ |
| | LASSO | $\mathcal{O}(G^2M_TM_R + G^3)$ |
| $\mathcal{H}_1$ | CSCD-H1 | $\mathcal{O}(G^2M_TM_RU + U^2(M_TM_R)^2I)$ |
| | GOMP | $\mathcal{O}(G^2M_TM_RU)$ |
| | MPIAA | $\mathcal{O}((G^4M_TM_R + M_TM_R^3)J)$ |
| | GLASSO | $\mathcal{O}(G^4M_TM_R + G^6)$ |

## B. Complexity Analysis

To evaluate the complexity of the proposed CSCD-based estimator, we consider the aforementioned grid-based methods comparison, i.e., the OMP-based, LASSO-based, and IAA-based estimators. In these comparisons, the continuous spatial space is discretized into $G$ grid points in $\mathcal{H}_0$ scenario and $G^2$ grid points in $\mathcal{H}_1$ scenario. The overall computational complexity of the algorithms depends on the number of iterations and the computational complexity per iteration. For the CSCD-H0, the computational complexity of the coarse and the refined estimation are $\mathcal{O}(GM_TM_R)$ and $\mathcal{O}(K_0(M_TM_R)^2I)$, respectively. The number of iterations is proportional to the number of direct paths $K_0$. Therefore, the overall computational complexity is $\mathcal{O}(GM_TM_RK_0 + K_0^2(M_TM_R)^2I)$. For the CSCD-H1, the number of iterations is proportional to $U = K_1 + K_0$, the overall computational complexity is $\mathcal{O}(G^2M_TM_RU + U^2(M_TM_R)^2I)$. The OMP-based estima-

This article has been accepted for publication in IEEE Transactions on Signal Processing. This is the author's version which has not been fully edited and content may change prior to final publication. Citation information: DOI 10.1109/TSP.2024.3384750



tors are simplified versions of CSCD without fine estimation. Therefore, the computational complexity is $\mathcal{O}(GM_TM_RK_0)$ under $\mathcal{H}_0$ and $\mathcal{O}(G^2M_TM_RU)$ under $\mathcal{H}_1$, respectively. For the IAA-based estimator,the overall computational complexity is $\mathcal{O}((G^2M_TM_R + M_TM_R^3)J)$ under $\mathcal{H}_0$ and $\mathcal{O}((G^4M_TM_R + M_TM_R^3)J)$ under $\mathcal{H}_1$, where $J$ denotes the number of iterations. For the LASSO-based estimator, the complexity is $\mathcal{O}(G^2M_TM_R + G^3)$ under $\mathcal{H}_0$ and $\mathcal{O}(G^4M_TM_R + G^6)$ under $\mathcal{H}_1$. We summarize the computational complexity of these methods in TABLE. I. It can be seen that the proposed method, due to the addition of refined angle estimation, has a slightly higher computational complexity than the OMP-based estimator, but it is significantly lower than that of the IAA-based and LASSO-based estimators. Moreover, we note that the computational complexity of the refined estimation in our proposed method is independent of grid density. We can achieve accurate estimation in the continuous domain with a coarser grid and a lower computational load through refined estimation.

## C. Estimation Performance

In this subsection, we verify the estimation performance of the proposed CSCD-H0 and CSCD-H1 algorithms. In the ULA array, we check the accuracy of direct path estimation in $\mathcal{H}_0$ scenario and first-order path estimation in $\mathcal{H}_1$ scenario in Fig. 6a and Fig. 6c. As expected, the RMSE of all estimators decreases as SNR grows, indicating that larger SNR leads to better accuracy in estimation. LASSO-based, IAA-based and OMP-based estimators suffer from off-grid issues, so their accuracy is consistently worse than that of the proposed algorithm. We notice that when the sparsity decreases ($K_0$ of Fig. 6a, or $K_1$ of Fig. 6c from 1 to 3), a decline in the accuracy could be observed. This phenomenon can be explained by many existing works in CS [43]: the CS-based estimators take advantage of the sparsity inside signal for estimation and the performance is getting worse as the sparsity decreases.

In the SLA array, we continue to observe that the proposed CSCD-based method exhibits improved angle estimation performance as the SNR increases. However, the RMSE of the OMP-based, IAA-based, and LASSO-based estimators remains largely unchanged in both $\mathcal{H}_0$ and $\mathcal{H}_1$ scenarios. This phenomenon can be attributed, in part, to our method of calculating RMSE. We assess accuracy based on (37) and (38), considering only paths that have been correctly identified, with estimation errors smaller than the array beamwidth. The on-grid methods experience a decrease in the rate of correctly identified paths compared to the ULA array, and they are constrained by grid resolution, which makes it challenging for RMSE to improve with increasing SNR.

However, unlike the ULA with half-lambda separation, the basis of the SLA array could have a large correlation. In Fig. 7a, given a direct path $\theta = 10°$, we computed its correlation $\langle \mathbf{a}(\theta), \mathbf{a}(\psi)\rangle$ with the basis $\psi \in [-90°, 90°]$ and observe that SLA has a narrower beamwidth but higher sidelobes. Given a first-order path $(\vartheta, \varphi) = (10°, -10°)$, the correlation $\langle \mathbf{a}_T(\vartheta) \circ \mathbf{a}_R(\varphi), \mathbf{a}(\psi)\rangle$ are plotted in Fig. 7b, where a distinct peak can be observed in SLA even if the signals are not matched. It indicates that, in SLA, the algorithm could make a mistake when doing basis selection and the performance of GLRT could be affected as well.

## D. Detection performance

In order to assess the detection performance of the proposed system, we need first to determine a method to set the detection threshold. In fact, unlike the ideal GLRT in (13), the GLRT-CSCD detector using CSCD-H0 and GCSD-H1 for estimation purposes no longer exhibits CFAR behavior, due to the inevitable errors occurring in the estimation procedures outlined in the previous section. It is thus necessary at first to undertake a sensitivity analysis, in order to assess if outright adoption of the detection threshold of the ideal GLRT, as defined in (19), yields a false alarm probability which at least preserves the order of magnitude of the designed value. To this end, we set a nominal value $P_{fa} = 10^{-3}$, select the corresponding detection threshold through inversion of (19), and then evaluate the false alarm probability achieved by the GLRT-LASSO, GLRT-IAA, GLRT-OMP and proposed GLRT-CSCD. The results are reported in Table II. Even though our analysis is far from being exhaustive, the results clearly show that the actual false alarm probability of GLRT-CSCD stays below the nominal level for a ULA configuration under all the inspected values of $\sigma_\alpha^2/\sigma^2$. The SLA configuration appears a little less favorable, especially as $K_0$ increases. This is due to the higher sidelobes that such an array configuration generates, with a consequent "spillover" of the direct paths into the first-order path subspace, but the order of magnitude of the actual $P_{fa}$ is again preserved. For the GLRT-OMP and GLRT-LASSO algorithms, the false alarm probability for both ULA and SLA is higher. And in the SLA, the order of magnitude of the actual $P_{fa}$ can no longer be preserved. Also, we have observed a significant increase in the case of GLRT-IAA method in SLA scenarios. The worst $P_{fa}$ is found in GLRT-IAA, at which point neither ULA nor SLA retains the magnitude of $P_{fa}$.

In Fig. 8, the $P_d$ of GLRT-LASSO, GLRT-IAA, GLRT-OMP, and GLRT-CSCD are compared with the upper bound. For the ULA results given by Fig. 8a, the detection performance of GLRT-CSCD with $K_1 = 1$ is close to the upper bound. As $K_1 = 3$ in Fig. 8b, the performance gap between the proposed detectors and the upper bound becomes larger due to the degradation in estimation performance. This is also validated by our RMSE simulation given by Fig. 6c. In the SLA, we can see from Fig. 8b, that the discrepancy between the proposed detectors and the upper bound is larger than that of ULA. The proposed GLRT-CSCD still benefits from a larger $K_1$ to achieve better detection performance. However, the angle estimation performance of the LASSO, IAA and OMP are much worse than that of the proposed algorithm, so its detection performance is considerably below the upper bound.

To compare detection performance across different array sizes, we set up simulations with $M_T = 3$, $M_R = 4$ ($M_TM_R = 12$), $M_T = 4$, $M_R = 6$ ($M_TM_R = 24$) and $M_T = 6$, $M_R = 8$ ($M_TM_R = 48$). For simplicity, we adopt

This article has been accepted for publication in IEEE Transactions on Signal Processing. This is the author's version which has not been fully edited and content may change prior to final publication. Citation information: DOI 10.1109/TSP.2024.3384750



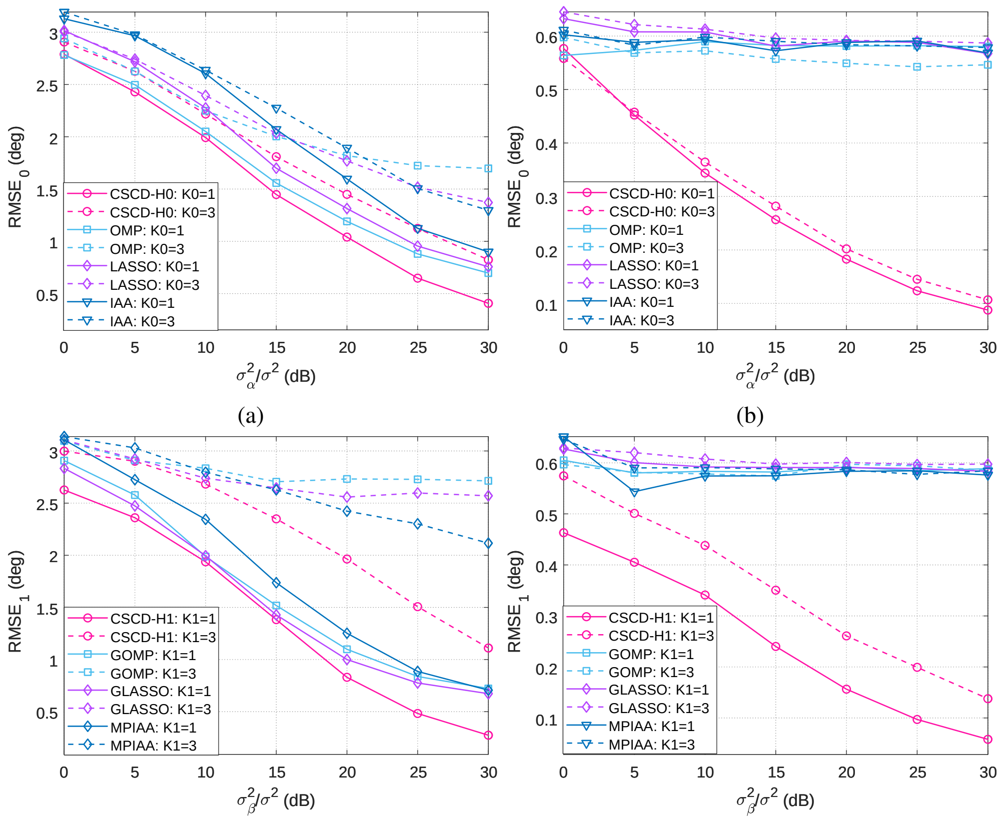


(a) (b)

(c) (d)

Fig. 6: Plots of RMSE:(a) $\mathrm{RMSE}_0$ in ULA, (b) $\mathrm{RMSE}_0$ in SLA, (c) $\mathrm{RMSE}_1$ in ULA, (d)$\mathrm{RMSE}_1$ in SLA.

TABLE II: Simulation of $P_{fa}$ with $M_T M_R = 48$

| Array | $K_0$ | GLRT-CSCD | | GLRT-OMP | | GLRT-LASSO | | GLRT-IAA | |
|---|---|---|---|---|---|---|---|---|---|
| | | $\frac{\sigma_\alpha^2}{\sigma^2}=0$ dB | $\frac{\sigma_\alpha^2}{\sigma^2}=20$ dB | $\frac{\sigma_\alpha^2}{\sigma^2}=0$ dB | $\frac{\sigma_\alpha^2}{\sigma^2}=20$ dB | $\frac{\sigma_\alpha^2}{\sigma^2}=0$ dB | $\frac{\sigma_\alpha^2}{\sigma^2}=20$ dB | $\frac{\sigma_\alpha^2}{\sigma^2}=0$ dB | $\frac{\sigma_\alpha^2}{\sigma^2}=20$ dB |
| ULA | 1 | $1.74\times10^{-4}$ | $3.00\times10^{-5}$ | $9.80\times10^{-3}$ | $2.30\times10^{-3}$ | $2.10\times10^{-3}$ | $5.40\times10^{-3}$ | $1.36\times10^{-2}$ | $2.64\times10^{-3}$ |
| | 3 | $3.00\times10^{-4}$ | $1.00\times10^{-5}$ | $5.80\times10^{-3}$ | $7.00\times10^{-4}$ | $1.12\times10^{-3}$ | $3.90\times10^{-3}$ | $1.44\times10^{-2}$ | $3.94\times10^{-3}$ |
| SLA | 1 | $4.50\times10^{-4}$ | $1.50\times10^{-4}$ | $2.12\times10^{-2}$ | $2.02\times10^{-2}$ | $1.05\times10^{-3}$ | $2.18\times10^{-1}$ | $1.08\times10^{-2}$ | $2.39\times10^{-1}$ |
| | 3 | $8.50\times10^{-4}$ | $5.30\times10^{-4}$ | $1.68\times10^{-2}$ | $5.70\times10^{-3}$ | $4.00\times10^{-4}$ | $1.64\times10^{-1}$ | $1.00\times10^{-2}$ | $2.41\times10^{-1}$ |

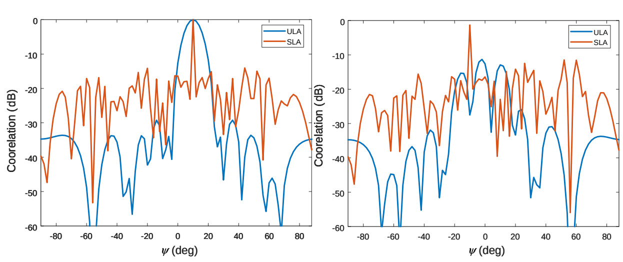


(a) (b)

Fig. 7: Comparison of (a) $\langle \mathbf{a}(\theta), \mathbf{a}(\psi)\rangle$ in $\mathcal{H}_0$ scenario, and (b) $\langle \mathbf{a}_T(\vartheta)\circ \mathbf{a}_R(\varphi), \mathbf{a}(\psi)\rangle$ in $\mathcal{H}_1$ scenario.

ULAs with half-wavelength element spacing and the detection performances are evaluated when $K_0 = 1$ and $K_1 = 1$. As reported in Fig. 9, the simulated performance is close to the upper bound given by the theoretical analysis. Detection performance improves with more degrees of freedom, even though the gain rapidly decreases once $M_T M_R$ is made sufficiently large as compared to the values of $K_0$ and $K_1$.

## E. Experimental results

Next, we evaluate the target detection performance of the proposed detector by using the experimental data. The data are obtained by a millimeter-wave $f_0 = 77$ GHz MIMO radar where $M_T = 8$ transmitting antenna and $M_R = 16$ receiving antenna, all evenly spaced. The spacing at the transmitter side is $4.5\lambda$, and the spacing at the receiver side is $4\lambda$. Fig.10a displays a typical automotive radar driving environment, where the road is flanked by concrete walls. The target is situated between these reflective surfaces, leading to multipath propagation of its echoes. Considering that the vehicle is in motion and all targets have a non-zero Doppler shift, to distinguish between stationary and moving targets in

This article has been accepted for publication in IEEE Transactions on Signal Processing. This is the author's version which has not been fully edited and content may change prior to final publication. Citation information: DOI 10.1109/TSP.2024.3384750



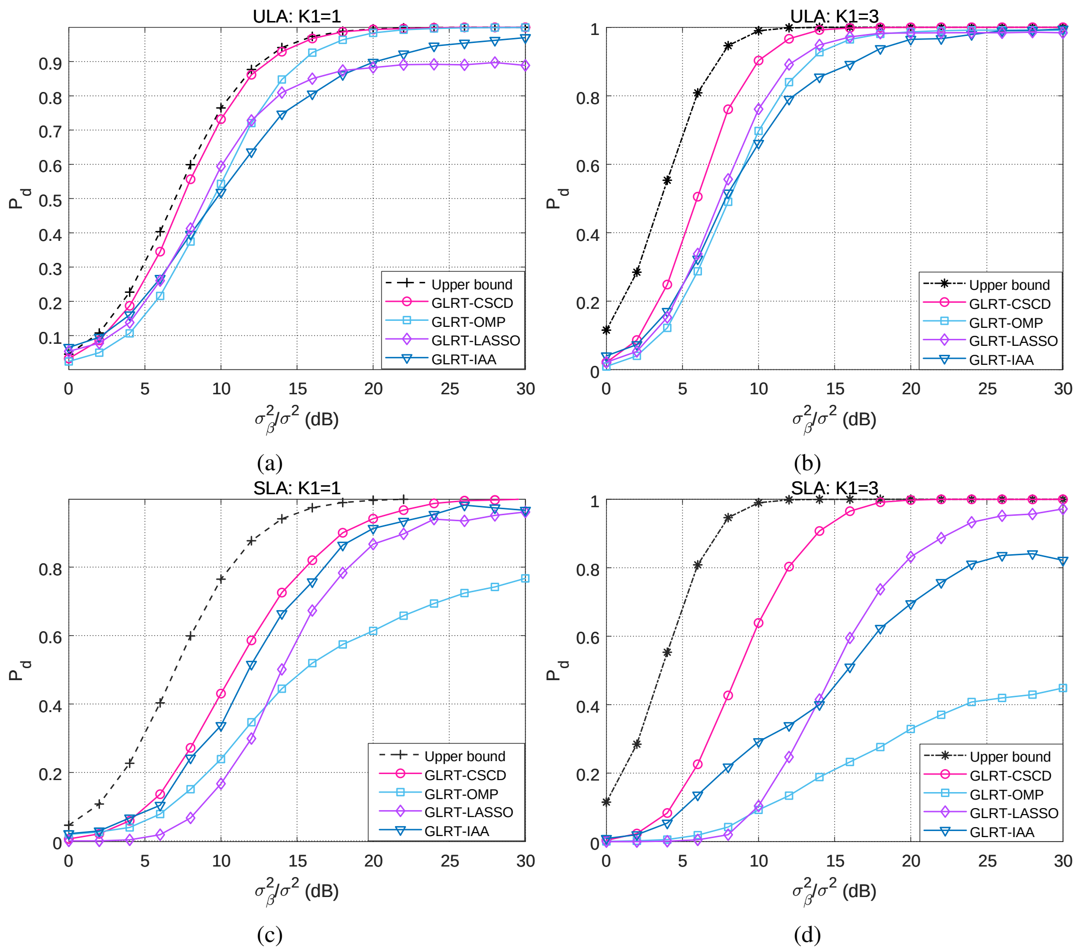


Fig. 8: $P_d$ versus $\sigma_\beta^2/\sigma^2$ for ULA with (a) $K_1 = 1$ and (b) $K_1 = 3$, SLA with (c) $K_1 = 1$ and (d) $K_1 = 3$.

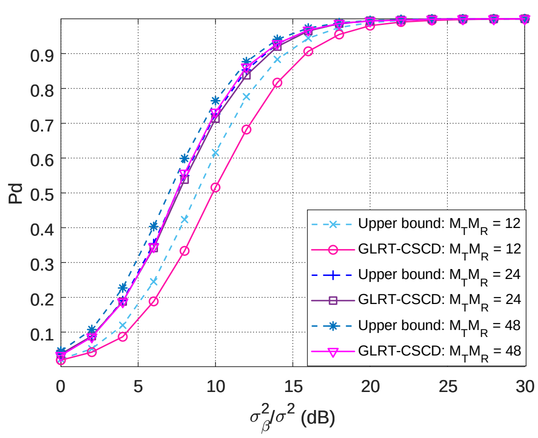


Fig. 9: $P_d$ versus $\sigma_\beta^2/\sigma^2$ for different $M_T M_R$.

the scene, automotive radar can utilize the vehicle's speed by an Inertial Measurement Unit (IMU). The IMU calculates the vehicle's velocity by measuring linear acceleration and angular velocity. Then, based on the estimated angle of the detection point, its relative radial velocity is projected along the direction of the vehicle's velocity. If the projected velocity matches the vehicle's own speed, the detection point is identified as a stationary target; otherwise, it is from a moving target. However, as illustrated in Fig.10b, ghosts caused by multipath lead to mismatches, resulting in the appearance of moving ghost targets, significantly impacting the vehicle's perception and decision-making process.

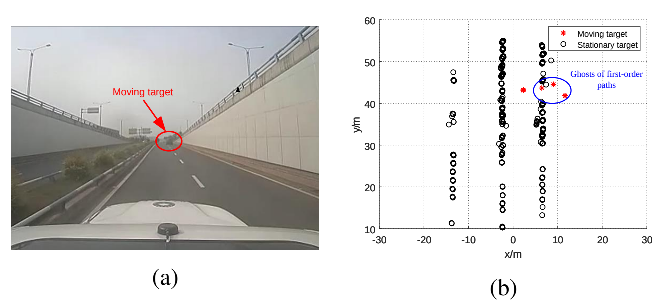


Fig. 10: Experimental scenario, (a) Photograph of the experimental scenario, (b) Points clouds with blue ellipse indicating ghosts induced by first-order paths

In Fig. 11, we employ the aforementioned GLRT-OMP, GLRT-LASSO, GLRT-IAA, and the proposed GLRT-CSCD to detect and eliminate ghost targets. It can be observed that the GLRT-OMP, GLRT-LASSO, and GLRT-IAA methods fail to successfully remove all ghost targets in the scene, they inadvertently remove some direct paths from stationary targets.

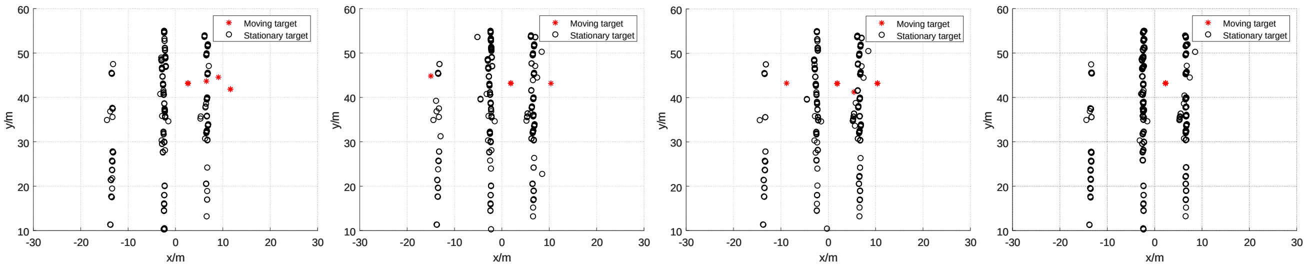


(a) (b) (c) (d)

Fig. 11: Detection and elimination of ghost targets using (a) GLRT-OMP, (b) GLRT-LASSO, (c) GLRT-IAA and (d) GLRT-CSCD.

In contrast, the proposed GLRT-CSCD method effectively eliminates all ghost targets while preserving the direct paths of stationary targets.

## VI. Conclusions

In this paper, we investigate the detection of ghost targets for automotive radar in the presence of multipaths. The existence of indirect paths is modeled as a binary composite hypothesis test and a GLRT detector is proposed to determine whether indirect paths exist in a delay-Doppler cell. If a cell contains indirect paths, the ghost targets could be removed and the desired direct paths can be preserved. Based on the theoretical analysis of the detection performance of GLRT under perfect angle estimation, we have derived a convex waveform optimization approach that can enhance detection performance. Considering practical scenarios with unknown angles of both direct and indirect paths, we propose a sparsity-enforced CS approach to estimate the angular parameters in the continuous domain. Simulation results indicate that the proposed algorithm outperforms on-grid estimators, thereby leading to better detection performance. The false alarm rate of the proposed detector could be controlled and the detection performance is close to the theoretical bound in the ULA case. Finally, the experimental results demonstrate the effectiveness of the proposed method.

## Appendix

### A. Derivation of $\mathbf{g}_0$ in (28) and $\mathbf{H}_0$ in (29)

For clarity, we drop the superscript $(t,i)$ and input variable of the functions in some of the following derivation, i.e. $F = F(\widehat{\boldsymbol{\Theta}}_0^{(t,i)})$ and $\bar{\mathbf{A}}_0 = \bar{\mathbf{A}}(\widehat{\boldsymbol{\Theta}}_0^{(t,i)})$.

Denote $F = \mathbf{f}^H\mathbf{f}$ with $\mathbf{f} = \bar{\boldsymbol{z}} - \bar{\mathbf{A}}\bar{\mathbf{A}}^\dagger\bar{\boldsymbol{z}}$, the gradient of $F$ with respect to $\boldsymbol{\Theta}_0 \in \mathbb{R}^{K_0\times 1}$ can be calculated by

$$\mathbf{g}_0 = \left[\frac{\partial F}{\partial\theta_1}, \frac{\partial F}{\partial\theta_2}, \ldots, \frac{\partial F}{\partial\theta_{K_0}}\right]^T, \tag{39}$$

where the $q$-th element $[\mathbf{g}_0]_q$ given as $\frac{\partial F}{\partial\theta_q} = 2\mathrm{Re}((\frac{\partial \mathbf{f}}{\partial\theta_q})^H\mathbf{f})$. Following the derivation in [49], we obtain

$$[\mathbf{g}_0]_q = -2\mathrm{Re}\left\{\mathrm{Tr}\{\bar{\mathbf{A}}_0^\dagger\bar{\boldsymbol{z}}\bar{\boldsymbol{z}}^H\boldsymbol{P}_0\bar{\mathbf{A}}_q\}\right\}, \tag{40}$$

where $\bar{\mathbf{A}}_q = \frac{\partial\bar{\mathbf{A}}_0}{\partial\theta_q} = [\mathbf{0}, \mathbf{0}, \ldots, \frac{\partial\bar{\mathbf{a}}}{\partial\theta_q}, \ldots, \mathbf{0}]$ with $\frac{\partial\bar{\mathbf{a}}}{\partial\theta_q} = \frac{\partial\bar{\mathbf{a}}(\theta_q)}{\partial\theta_q}$.

The Hessian $\mathbf{H}_0$ denotes approximate second order partial derivative of $F$ with respect to $\boldsymbol{\Theta}_0$. In this matrix, the $(q,p)$-th element is denoted as $[\mathbf{H}_0]_{q,p} = 2\mathrm{Re}\left\{\left(\frac{\partial\mathbf{f}}{\partial\theta_q}\right)^H\frac{\partial\mathbf{f}}{\partial\theta_p}\right\}$ and can be calculated as follows

$$\begin{aligned}[\mathbf{H}_0]_{q,p} =& 2\mathrm{Re}\left\{\mathrm{Tr}\{\bar{\mathbf{A}}_p\bar{\mathbf{A}}_0^\dagger\bar{\boldsymbol{z}}\bar{\boldsymbol{z}}^H(\bar{\mathbf{A}}_0^\dagger)^H\bar{\mathbf{A}}_q^H\boldsymbol{P}_0\}\right\} \\ &+ 2\mathrm{Re}\left\{\mathrm{Tr}\{\bar{\mathbf{A}}_p^H\boldsymbol{P}_0\bar{\boldsymbol{z}}\bar{\boldsymbol{z}}^H\boldsymbol{P}_0\bar{\mathbf{A}}_q\bar{\mathbf{A}}_0^\dagger(\bar{\mathbf{A}}_0^\dagger)^H\}\right\}.\end{aligned} \tag{41}$$

Defining a partial matrix $\mathbf{D}_0 = \left[\frac{\partial\bar{\mathbf{a}}}{\partial\theta_1}, \frac{\partial\bar{\mathbf{a}}}{\partial\theta_2}, \ldots, \frac{\partial\bar{\mathbf{a}}}{\partial\theta_{K_0}}\right]$, then the matrix form of $\mathbf{g}$ and $\mathbf{H}_0$ can be given by (28) and (29), respectively.

### B. Derivation of $\mathbf{g}$'s in (34) and $\mathbf{H}$'s in (35)

For clarity, we drop the superscript and input variable of the functions in some of the following derivations, i.e. $\bar{F} = \bar{F}(\bar{\boldsymbol{\Theta}}^{(t,i)})$ and $\bar{\mathbf{A}} = \bar{\mathbf{A}}(\bar{\boldsymbol{\Theta}}^{(t,i)}, \bar{\boldsymbol{\Phi}}^{(t,i)})$. In the following, we derive the matrix expression of $\mathbf{g}_T$ and $\mathbf{H}_{\mathrm{TT}}$, the derivation for $\mathbf{g}_{\mathrm{R}}$, $\mathbf{g}_0'$, $\mathbf{H}_{\mathrm{TR}}$, $\mathbf{H}_{\mathrm{RR}}$, $\mathbf{H}_{\mathrm{RT}}$, $\mathbf{H}_{0\mathrm{T}}$, $\mathbf{H}_{\mathrm{T}0}$, $\mathbf{H}_{\mathrm{R}0}$, $\mathbf{H}_{0\mathrm{R}}$, $\mathbf{H}_{00}$ follow similar arguments and are omitted for brevity. Similar with (40), we know the $q$-th element of $\mathbf{g}_T$ can be given as

$$\begin{aligned}[\mathbf{g}_{\mathrm{T}}]_q &= -2\mathrm{Re}\{\mathrm{Tr}\{\bar{\mathbf{A}}^\dagger\bar{\boldsymbol{z}}\bar{\boldsymbol{z}}^H\boldsymbol{P}_1\bar{\mathbf{A}}_q'\}\}, \\ &= -2\mathrm{Re}\left\{\mathrm{Tr}\{\boldsymbol{\Gamma}\bar{\mathbf{A}}_q'\}\right\},\end{aligned} \tag{42}$$

where $\boldsymbol{\Gamma} = \bar{\mathbf{A}}^\dagger\bar{\boldsymbol{z}}\bar{\boldsymbol{z}}^H\boldsymbol{P}_1 \in \mathbb{C}^{(2K_1+K_0)\times M_TM_R}$, $\bar{\mathbf{A}}_q' = \frac{\partial\bar{\mathbf{A}}}{\partial\vartheta_q} = [\mathbf{0}, \mathbf{0}, \ldots, \frac{\partial\mathbf{a}_1}{\partial\vartheta_q}, \ldots, \mathbf{0}, \ldots, \frac{\partial\mathbf{a}_2}{\partial\vartheta_q}, \ldots, \mathbf{0}]$ with $\frac{\partial\mathbf{a}_1}{\partial\vartheta_q} = \boldsymbol{\Sigma}_x^{1/2}\frac{\partial\mathbf{a}_T(\vartheta_q)\otimes\mathbf{a}_R(\varphi_q)}{\partial\vartheta_q}$ and $\frac{\partial\mathbf{a}_2}{\partial\vartheta_q} = \boldsymbol{\Sigma}_x^{1/2}\frac{\partial\mathbf{a}_T(\varphi_q)\otimes\mathbf{a}_R(\vartheta_q)}{\partial\vartheta_q}$. We divide the matrix $\boldsymbol{\Gamma}$ into three submatrices, denoted as $\boldsymbol{\Gamma} = [\boldsymbol{\Gamma}_1, \boldsymbol{\Gamma}_2, \boldsymbol{\Gamma}_0]$, where $\boldsymbol{\Gamma}_1, \boldsymbol{\Gamma}_2 \in \mathbb{C}^{K_1\times M_TM_R}$, $\boldsymbol{\Gamma}_0 \in \mathbb{C}^{K_0\times M_TM_R}$. Then (42) can be rewritten as

$$[\mathbf{g}_{\mathrm{T}}]_q = -2\mathrm{Re}\left\{\boldsymbol{\Gamma}_1^T(q)(\frac{\partial\mathbf{a}_1}{\partial\vartheta_q})^T + \boldsymbol{\Gamma}_2^T(q)(\frac{\partial\mathbf{a}_2}{\partial\vartheta_q})^T\right\}, \tag{43}$$

where $\boldsymbol{\Gamma}_1^T(q)$ and $\boldsymbol{\Gamma}_2^T(q)$ denote the $q$ row of $\boldsymbol{\Gamma}_1$ and $\boldsymbol{\Gamma}_2$, respectively. Define two partial matrices: $\mathbf{D}_{\mathrm{T}1} = \left[\frac{\partial\mathbf{a}_1}{\partial\vartheta_1}, \frac{\partial\mathbf{a}_1}{\partial\vartheta_2}, \ldots, \frac{\partial\mathbf{a}_1}{\partial\vartheta_{K_1}}\right]$, $\mathbf{D}_{\mathrm{T}2} = \left[\frac{\partial\mathbf{a}_2}{\partial\vartheta_2}, \frac{\partial\mathbf{a}_2}{\partial\vartheta_2}, \ldots, \frac{\partial\mathbf{a}_2}{\partial\vartheta_{K_1}}\right]$. We can then obtain the matrix form of $\mathbf{g}_{\mathrm{T}}$ given by

$$\mathbf{g}_{\mathrm{T}} = -2\mathrm{Re}\{\mathrm{diag}\{\Gamma_1\mathbf{D}_{\mathrm{T}1} + \Gamma_2\mathbf{D}_{\mathrm{T}2}\}\}. \tag{44}$$

Similarly, we define $\mathbf{D}_{\mathrm{R1}} = \left[\frac{\partial \mathbf{a}_1}{\partial \varphi_1}, \frac{\partial \mathbf{a}_1}{\partial \varphi_2}, \ldots, \frac{\partial \mathbf{a}_1}{\partial \varphi_{K_1}}\right]$, $\mathbf{D}_{\mathrm{R2}} = \left[\frac{\partial \mathbf{a}_2}{\partial \varphi_2}, \frac{\partial \mathbf{a}_2}{\partial \varphi_2}, \ldots, \frac{\partial \mathbf{a}_2}{\partial \varphi_{K_1}}\right]$ and $\mathbf{D}_0 = \left[\frac{\partial \bar{\mathbf{a}}}{\partial \theta_1}, \frac{\partial \bar{\mathbf{a}}}{\partial \theta_2}, \ldots, \frac{\partial \bar{\mathbf{a}}}{\partial \theta_{K_0}}\right]$, and obtain

$$\begin{aligned} \mathbf{g}_{\mathrm{R}} &= -2\mathrm{Re}\{\mathrm{diag}\{\Gamma_1 \mathbf{D}_{\mathrm{R1}} + \Gamma_2 \mathbf{D}_{\mathrm{R2}}\}\}, && (45)\\ \mathbf{g}_0' &= -2\mathrm{Re}\{\mathrm{diag}\{\Gamma_0 \mathbf{D}_0\}\}. && (46) \end{aligned}$$

The Hessian $\mathbf{H}_{\mathrm{TT}}$ denotes second order partial derivative with respect to $\mathbf{\Theta}_1$, in which the $(q,p)$-th element is

$$\begin{aligned} [\mathbf{H}_{\mathrm{TT}}]_{q,p} =& 2\mathrm{Re}\left\{\mathrm{Tr}\{\bar{\mathbf{A}}_p' \bar{\mathbf{A}}^\dagger \bar{\boldsymbol{z}} \bar{\boldsymbol{z}}^H (\bar{\mathbf{A}}^\dagger)^H (\bar{\mathbf{A}}_q')^H \boldsymbol{P}_1\}\right\} \\ &+ 2\mathrm{Re}\left\{\mathrm{Tr}\{(\bar{\mathbf{A}}_p')^H \boldsymbol{P}_1 \bar{\boldsymbol{z}} \bar{\boldsymbol{z}}^H \boldsymbol{P}_1 \bar{\mathbf{A}}_q' \bar{\mathbf{A}}^\dagger (\bar{\mathbf{A}}^\dagger)^H\}\right\}, \end{aligned} \tag{47}$$

where the first item

$$\begin{aligned} &\mathrm{Tr}\{\bar{\mathbf{A}}_p' \bar{\mathbf{A}}^\dagger \bar{\boldsymbol{z}} \bar{\boldsymbol{z}}^H (\bar{\mathbf{A}}^\dagger)^H (\bar{\mathbf{A}}_q')^H \boldsymbol{P}_1\} \\ &= \mathbf{S}_{p,q} (\frac{\partial \mathbf{a}_1}{\partial \vartheta_q})^H \boldsymbol{P}_1 \frac{\partial \mathbf{a}_1}{\partial \vartheta_p} + [\mathbf{S}]_{p,q+K_1} (\frac{\partial \mathbf{a}_2}{\partial \vartheta_q})^H \boldsymbol{P}_1 \frac{\partial \mathbf{a}_1}{\partial \vartheta_p} \\ &+ [\mathbf{S}]_{p+K_1,q} (\frac{\partial \mathbf{a}_1}{\partial \vartheta_q})^H \boldsymbol{P}_1 \frac{\partial \mathbf{a}_2}{\partial \vartheta_p} + [\mathbf{S}]_{p+K_1,q+K_1} (\frac{\partial \mathbf{a}_2}{\partial \vartheta_q})^H \boldsymbol{P}_1 \frac{\partial \mathbf{a}_2}{\partial \vartheta_p} \end{aligned}$$

with $\mathbf{S} = \bar{\mathbf{A}}^\dagger \bar{\boldsymbol{z}} \bar{\boldsymbol{z}}^H (\bar{\mathbf{A}}^\dagger)^H$, and the second item can be rewritten as

$$\begin{aligned} &\mathrm{Tr}\{(\bar{\mathbf{A}}_p')^H \boldsymbol{P}_1 \bar{\boldsymbol{z}} \bar{\boldsymbol{z}}^H \boldsymbol{P}_1 \bar{\mathbf{A}}_q' \bar{\mathbf{A}}^\dagger (\bar{\mathbf{A}}^\dagger)^H\} \\ &= [\mathbf{C}]_{q,p} (\frac{\partial \mathbf{a}_1}{\partial \vartheta_p})^H \mathbf{X} \frac{\partial \mathbf{a}_1}{\partial \vartheta_q} + [\mathbf{C}]_{q+K_1,p} (\frac{\partial \mathbf{a}_1}{\partial \vartheta_p})^H \mathbf{X} \frac{\partial \mathbf{a}_2}{\partial \vartheta_q} \\ &+ [\mathbf{C}]_{q,p+K_1} (\frac{\partial \mathbf{a}_2}{\partial \vartheta_p})^H \mathbf{X} \frac{\partial \mathbf{a}_1}{\partial \vartheta_q} + [\mathbf{C}]_{q+K_1,p+K_1} (\frac{\partial \mathbf{a}_2}{\partial \vartheta_p})^H \mathbf{X} \frac{\partial \mathbf{a}_2}{\partial \vartheta_q} \end{aligned}$$

with $\mathbf{X} = \boldsymbol{P}_1 \bar{\boldsymbol{z}} \bar{\boldsymbol{z}}^H \boldsymbol{P}_1$ and $\mathbf{C} = \bar{\mathbf{A}}^\dagger (\bar{\mathbf{A}}^\dagger)^H$. To represent $\mathbf{H}_{\mathrm{TT}}$ in matrix form, we divide matrices $\mathbf{S}$ and $\mathbf{C}$ into

$$\mathbf{S} = \begin{bmatrix} \mathbf{S}_1 & \mathbf{S}_{10} \\ \mathbf{S}_{01} & \mathbf{S}_0 \end{bmatrix}, \tag{48}$$

$$\mathbf{C} = \begin{bmatrix} \mathbf{C}_1 & \mathbf{C}_{10} \\ \mathbf{C}_{01} & \mathbf{C}_0 \end{bmatrix}, \tag{49}$$

where $\mathbf{S}_1, \mathbf{C}_1 \in \mathbb{C}^{2K_1 \times 2K_1}$,$\mathbf{S}_{10}, \mathbf{C}_{10} \in \mathbb{C}^{2K_1 \times K_0}$, $\mathbf{S}_{01}, \mathbf{C}_{01} \in \mathbb{C}^{K_0 \times 2K_1}$ and $\mathbf{S}_0, \mathbf{C}_0 \in \mathbb{C}^{K_0 \times K_0}$. Then, we obtain

$$\begin{aligned} \mathbf{H}_{\mathrm{TT}} &= 2\mathrm{Re}\left\{\mathbf{E}_{\mathrm{h}} (\mathbf{D}_{\mathrm{T}})^H \boldsymbol{P}_1 \mathbf{D}_{\mathrm{T}} \odot \mathbf{S}_1^T \mathbf{E}_{\mathrm{h}}^T\right\} \\ &+ 2\mathrm{Re}\left\{\mathbf{E}_{\mathrm{h}} ((\mathbf{D}_{\mathrm{T}})^H \mathbf{X} \mathbf{D}_{\mathrm{T}})^T \odot \mathbf{C}_1 \mathbf{E}_{\mathrm{h}}^T\right\}, \end{aligned} \tag{50}$$

where $\mathbf{E}_{\mathrm{h}} = [\boldsymbol{I}_{K_1}, \boldsymbol{I}_{K_1}] \in \mathbb{R}^{K_1 \times 2K_1}$, $\mathbf{D}_{\mathrm{T}} = [\mathbf{D}_{\mathrm{T1}}, \mathbf{D}_{\mathrm{T2}}]$. Similarly, we define $\mathbf{D}_{\mathrm{R}} = [\mathbf{D}_{\mathrm{R1}}, \mathbf{D}_{\mathrm{R2}}]$ and obtain

$$\begin{aligned} \mathbf{H}_{\mathrm{TR}} &= 2\mathrm{Re}\left\{\mathbf{E}_{\mathrm{h}} (\mathbf{D}_{\mathrm{T}})^H \boldsymbol{P}_1 \mathbf{D}_{\mathrm{R}} \odot \mathbf{S}^T \mathbf{E}_{\mathrm{h}}^T\right\} \\ &+ 2\mathrm{Re}\left\{\mathbf{E}_{\mathrm{h}} ((\mathbf{D}_{\mathrm{R}})^H \mathbf{X} \mathbf{D}_{\mathrm{T}})^T \odot \mathbf{C} \mathbf{E}_{\mathrm{h}}^T\right\}, \end{aligned} \tag{51}$$

$$\begin{aligned} \mathbf{H}_{\mathrm{RT}} &= 2\mathrm{Re}\left\{\mathbf{E}_{\mathrm{h}} (\mathbf{D}_{\mathrm{R}})^H \boldsymbol{P}_1 \mathbf{D}_{\mathrm{T}} \odot \mathbf{S}_1^T \mathbf{E}_{\mathrm{h}}^T\right\} \\ &+ 2\mathrm{Re}\left\{\mathbf{E}_{\mathrm{h}} ((\mathbf{D}_{\mathrm{T}})^H \mathbf{X} \mathbf{D}_{\mathrm{R}})^T \odot \mathbf{C}_1 \mathbf{E}_{\mathrm{h}}^T\right\}, \end{aligned} \tag{52}$$

$$\begin{aligned} \mathbf{H}_{\mathrm{RR}} &= 2\mathrm{Re}\left\{\mathbf{E}_{\mathrm{h}} (\mathbf{D}_{\mathrm{R}})^H \boldsymbol{P}_1 \mathbf{D}_{\mathrm{R}} \odot \mathbf{S}_1^T \mathbf{E}_{\mathrm{h}}^T\right\} \\ &+ 2\mathrm{Re}\left\{\mathbf{E}_{\mathrm{h}} ((\mathbf{D}_{\mathrm{R}})^H \mathbf{X} \mathbf{D}_{\mathrm{R}})^T \odot \mathbf{C}_1 \mathbf{E}_{\mathrm{h}}^T\right\}, \end{aligned} \tag{53}$$

$$\begin{aligned} \mathbf{H}_{\mathrm{T0}} &= 2\mathrm{Re}\left\{\mathbf{E}_{\mathrm{h}} \left((\mathbf{D}_{\mathrm{T}})^H \boldsymbol{P}_1 \mathbf{D}_0 \odot \mathbf{S}_{01}^T\right)\right\} \\ &+ 2\mathrm{Re}\left\{\mathbf{E}_{\mathrm{h}} \left(((\mathbf{D}_0)^H \mathbf{X} \mathbf{D}_T)^T \odot \mathbf{C}_{10}\right)\right\}, \end{aligned} \tag{54}$$

$$\begin{aligned} \mathbf{H}_{\mathrm{R0}} &= 2\mathrm{Re}\left\{\mathbf{E}_{\mathrm{h}} \left((\mathbf{D}_{\mathrm{R}})^H \boldsymbol{P}_1 \mathbf{D}_0 \odot \mathbf{S}_{01}^T\right)\right\} \\ &+ 2\mathrm{Re}\left\{\mathbf{E}_{\mathrm{h}} \left(((\mathbf{D}_0)^H \mathbf{X} \mathbf{D}_R)^T \odot \mathbf{C}_{10}\right)\right\}, \end{aligned} \tag{55}$$

$$\begin{aligned} \mathbf{H}_{\mathrm{0T}} &= 2\mathrm{Re}\left\{\left((\mathbf{D}_0)^H \boldsymbol{P}_1 \mathbf{D}_{\mathrm{T}} \odot \mathbf{S}_{10}^T\right) \mathbf{E}_{\mathrm{h}}^T\right\} \\ &+ 2\mathrm{Re}\left\{\left(((\mathbf{D}_{\mathrm{T}})^H \mathbf{X} \mathbf{D}_0)^T \odot \mathbf{C}_{01}\right) \mathbf{E}_{\mathrm{h}}^T\right\}, \end{aligned} \tag{56}$$

$$\begin{aligned} \mathbf{H}_{\mathrm{0R}} &= 2\mathrm{Re}\left\{\left((\mathbf{D}_0)^H \boldsymbol{P}_1 \mathbf{D}_{\mathrm{R}} \odot \mathbf{S}_{10}^T\right) \mathbf{E}_{\mathrm{h}}^T\right\} \\ &+ 2\mathrm{Re}\left\{\left(((\mathbf{D}_{\mathrm{R}})^H \mathbf{X} \mathbf{D}_0)^T \odot \mathbf{C}_{01}\right) \mathbf{E}_{\mathrm{h}}^T\right\}, \end{aligned} \tag{57}$$

$$\begin{aligned} \mathbf{H}_{00} &= 2\mathrm{Re}\left\{\mathbf{D}_0^H \boldsymbol{P}_1 \mathbf{D}_0 \odot \mathbf{S}_0^T\right\} \\ &+ 2\mathrm{Re}\left\{(\mathbf{D}_0^H \mathbf{X} \mathbf{D}_0)^T \odot \mathbf{C}_0\right\}. \end{aligned} \tag{58}$$

## REFERENCES


[1] S. M. Patole, M. Torlak, D. Wang, and M. Ali, "Automotive radars: A review of signal processing techniques," *IEEE Signal Processing Magazine*, vol. 34, no. 2, pp. 22–35, 2017.

[2] F. Engels, P. Heidenreich, A. M. Zoubir, F. K. Jondral, and M. Wintermantel, "Advances in automotive radar: A framework on computationally efficient high-resolution frequency estimation," *IEEE Signal Processing Magazine*, vol. 34, no. 2, pp. 36–46, 2017.

[3] F. Roos, J. Bechter, C. Knill, B. Schweizer, and C. Waldschmidt, "Radar sensors for autonomous driving: Modulation schemes and interference mitigation," *IEEE Microwave Magazine*, vol. 20, no. 9, pp. 58–72, 2019.

[4] C. Waldschmidt, J. Hasch, and W. Menzel, "Automotive radar — from first efforts to future systems," *IEEE Journal of Microwaves*, vol. 1, no. 1, pp. 135–148, 2021.

[5] J. Li and P. Stoica, "MIMO radar with colocated antennas," *IEEE Signal Processing Magazine*, vol. 24, no. 5, pp. 106–114, 2007.

[6] S. Sun, A. P. Petropulu, and H. V. Poor, "MIMO radar for advanced driver-assistance systems and autonomous driving: Advantages and challenges," *IEEE Signal Processing Magazine*, vol. 37, no. 4, pp. 98–117, 2020.

[7] X. Hu, Y. Li, M. Lu, Y. Wang, and X. Yang, "A multi-carrier-frequency random-transmission chirp sequence for TDM MIMO automotive radar," *IEEE Transactions on Vehicular Technology*, vol. 68, no. 4, pp. 3672–3685, 2019.

[8] A. Kamann, P. Held, F. Perras, P. Zaumseil, T. Brandmeier, and U. T. Schwarz, "Automotive radar multipath propagation in uncertain environments," in *2018 21st International Conference on Intelligent Transportation Systems (ITSC)*, 2018, pp. 859–864.

[9] T. Visentin, J. Hasch, and T. Zwick, "Analysis of multipath and DOA detection using a fully polarimetric automotive radar," in *2017 European Radar Conference (EURAD)*, 2017, pp. 45–48.

[10] K. Sabet, A. Sabet, J. Kral, and C. Woischwill, "Hybrid computer simulation of automotive radar systems in high multipath environments," in *2020 IEEE International Symposium on Antennas and Propagation and North American Radio Science Meeting*. Montreal, QC, Canada: IEEE, Jul. 2020, pp. 1561–1562.

[11] O. Longman, S. Villeval, and I. Bilik, "Multipath ghost targets mitigation in automotive environments," in *2021 IEEE Radar Conference (RadarConf21)*. Atlanta, GA, USA: IEEE, May 2021, pp. 1–5.

[12] M. Levy-Israel, I. Bilik, and J. Tabrikian, "MCRB on DOA estimation for automotive MIMO radar in the presence of multipath," *IEEE Transactions on Aerospace and Electronic Systems*, pp. 1–12, 2023.

[13] R. Feng, E. D. Greef, M. Rykunov, H. Sahli, S. Pollin, and A. Bourdoux, "Multipath ghost recognition for indoor MIMO radar," *IEEE Transactions on Geoscience and Remote Sensing*, vol. 60, pp. 1–10, 2022.

[14] F. Roos, M. Sadeghi, J. Bechter, N. Appenrodt, J. Dickmann, and C. Waldschmidt, "Ghost target identification by analysis of the Doppler distribution in automotive scenarios," in *2017 18th International Radar Symposium (IRS)*, 2017, pp. 1–9.

[15] X. Qiu, X. Zhang, K. Huo, and W. Jiang, "Quartic riemannian adaptive regularization with cubics for radar waveform design," *IEEE Transactions on Aerospace and Electronic Systems*, vol. 59, no. 6, pp. 7514–7528, 2023.

[16] W. Li, Q. Wan, Y. Zhi, H. Peng, and J. Mao, "A fans-shaped beam antenna design for overcoming multipath effects for 77GHz FMCW-MIMO radar," in *2021 IEEE MTT-S International Wireless Symposium (IWS)*. Nanjing, China: IEEE, May 2021, pp. 1–3.

[17] M. Manzoni, S. Tebaldini, A. V. Monti-Guarnieri, and C. M. Prati, "Multipath in automotive MIMO SAR imaging," *IEEE Transactions on Geoscience and Remote Sensing*, vol. 61, pp. 1–12, 2023.

[18] Y. Jia, Y. Guo, S. Chen, R. Song, G. Wang, X. Zhong, C. Yan, and G. Cui, "Multipath ghost and side/grating lobe suppression based on stacked generative adversarial nets in MIMO through-wall radar imaging," *IEEE Access*, vol. 7, pp. 143 367–143 380, 2019.

[19] R. Feng, E. De Greef, M. Rykunov, H. Sahli, S. Pollin, and A. Bourdoux, "Multipath ghost classification for MIMO radar using deep neural networks," in *2022 IEEE Radar Conference (RadarConf22)*, 2022, pp. 1–6.

[20] P. Wu, J. Chen, S. Guo, G. Cui, L. Kong, and X. Yang, "NLOS positioning for building layout and target based on association and hypothesis method," *IEEE Transactions on Geoscience and Remote Sensing*, vol. 61, pp. 1–13, 2023.

[21] J. Chen, S. Guo, H. Luo, N. Li, and G. Cui, "Non-line-of-sight multi-target localization algorithm for driver-assistance radar system," *IEEE Transactions on Vehicular Technology*, vol. 72, no. 4, pp. 5332–5337, 2023.

[22] S. Buzzi, E. Grossi, M. Lops, and L. Venturino, "Foundations of MIMO radar detection aided by reconfigurable intelligent surfaces," *IEEE Transactions on Signal Processing*, vol. 70, pp. 1749–1763, 2022.

[23] F. Engels, M. Wintermantel, and P. Heidenreich, "Automotive MIMO radar angle estimation in the presence of multipath," in *2017 European Radar Conference (EURAD)*. Nuremberg: IEEE, Oct. 2017, pp. 82–85.

[24] B. Li, S. Wang, J. Zhang, X. Cao, and C. Zhao, "Ultra-fast accurate AoA estimation via automotive massive-MIMO radar," *IEEE Transactions on Vehicular Technology*, vol. 71, no. 2, pp. 1172–1186, 2022.

[25] X. Zhang, L. Xu, L. Xu, and D. Xu, "Direction of departure (DOD) and direction of arrival (DOA) estimation in MIMO radar with reduced-dimension MUSIC," *IEEE Communications Letters*, vol. 14, no. 12, pp. 1161–1163, 2010.

[26] H. Jiang, J.-K. Zhang, and K. M. Wong, "Joint DOD and DOA estimation for bistatic MIMO radar in unknown correlated noise," *IEEE Transactions on Vehicular Technology*, vol. 64, no. 11, pp. 5113–5125, 2015.

[27] H. Luo, Z. Zhu, M. Jiang, S. Guo, and G. Cui, "An effective multipath ghost recognition method for sparse MIMO radar," *IEEE Transactions on Geoscience and Remote Sensing*, vol. 61, pp. 1–11, 2023.

[28] Y. Li and X. Shang, "Multipath ghost target identification for automotive MIMO radar," in *2022 IEEE 96th Vehicular Technology Conference (VTC2022-Fall)*. London, United Kingdom: IEEE, Sep. 2022, pp. 1–5.

[29] Z. Zhu, S. Guo, J. Chen, S. Xue, Z. Xu, P. Wu, G. Cui, and L. Kong, "Non-line-of-sight targets localization algorithm via joint estimation of DoD and DoA," *IEEE Transactions on Instrumentation and Measurement*, vol. 72, pp. 1–11, 2023.

[30] L. Zheng, A. Maleki, H. Weng, X. Wang, and T. Long, "Does $\ell_p$ -minimization outperform $\ell_1$ -minimization?" *IEEE Transactions on Information Theory*, vol. 63, no. 11, pp. 6896–6935, 2017.

[31] Q. Xie, X. Pan, M. Huang, J. Chen, and S. Xiao, "Sparsity-based Direction-of-Departure and Direction-of-Arrival estimation for bistatic Multiple-Input Multiple-Output radar," *IEEE Access*, vol. 7, pp. 118 826–118 838, 2019.

[32] T. Strohmer and B. Friedlander, "Analysis of sparse MIMO radar," *Applied and Computational Harmonic Analysis*, vol. 37, no. 3, pp. 361–388, 2014. [Online]. Available: https://www.sciencedirect.com/science/article/pii/S1063520314000037

[33] B. Jokanovic and M. Amin, "Reduced interference sparse time-frequency distributions for compressed observations," *IEEE Transactions on Signal Processing*, vol. 63, no. 24, pp. 6698–6709, 2015.

[34] L. Zheng and X. Wang, "Super-resolution delay-Doppler estimation for OFDM passive radar," *IEEE Transactions on Signal Processing*, vol. 65, no. 9, pp. 2197–2210, May 2017.

[35] H. Rohling and M.-M. Meinecke, "Waveform design principles for automotive radar systems," in *2001 CIE International Conference on Radar Proceedings (Cat No.01TH8559)*, 2001, pp. 1–4.

[36] M. Kronauge and H. Rohling, "New chirp sequence radar waveform," *IEEE Transactions on Aerospace and Electronic Systems*, vol. 50, no. 4, pp. 2870–2877, Oct. 2014.

[37] K. Doris, A. Filippi, and F. Jansen, "Reframing fast-chirp FMCW transceivers for future automotive radar : The pathway to higher resolution," *IEEE Solid-State Circuits Magazine*, vol. 14, no. 2, pp. 44–55, 2022.

[38] X. Wang, M. Jia, X. Meng, and T. Zhang, "Multipath ghosts mitigation for radar-based positioning systems," in *2022 IEEE 96th Vehicular Technology Conference (VTC2022-Fall)*. London, United Kingdom: IEEE, Sep. 2022, pp. 1–6.

[39] A. B. Baral and M. Torlak, "Joint Doppler frequency and direction of arrival estimation for TDM MIMO automotive radars," *IEEE Journal of Selected Topics in Signal Processing*, vol. 15, no. 4, pp. 980–995, 2021.

[40] P. Wang, P. Boufounos, H. Mansour, and P. V. Orlik, "Slow-time MIMO-FMCW automotive radar detection with imperfect waveform separation," in *ICASSP 2020 - 2020 IEEE International Conference on Acoustics, Speech and Signal Processing (ICASSP)*, 2020, pp. 8634–8638.

[41] L. L. Scharf and B. Friedlander, "Matched subspace detectors," *IEEE Transactions on Signal Processing*, vol. 42, no. 8, pp. 2146–2157, 1994.

[42] E. L. Lehmann and J. P. Romano, *Uniformly Most Powerful Tests*. New York, NY: Springer New York, 2005, pp. 56–109.

[43] Z. Yang and L. Xie, "Exact joint sparse frequency recovery via optimization methods," *IEEE Transactions on Signal Processing*, vol. 64, no. 19, pp. 5145–5157, 2016.

[44] A. Aich and P. Palanisamy, "On-grid DOA estimation method using orthogonal matching pursuit," in *2017 International Conference on Signal Processing and Communication (ICSPC)*, 2017, pp. 483–487.

[45] H. P. Gavin, "The levenberg-marquardt algorithm for nonlinear least squares curve-fitting problems," *Department of civil and environmental engineering, Duke University*, vol. 19, 2019.

[46] W. Roberts, P. Stoica, J. Li, T. Yardibi, and F. A. Sadjadi, "Iterative adaptive approaches to mimo radar imaging," *IEEE Journal of Selected Topics in Signal Processing*, vol. 4, no. 1, pp. 5–20, 2010.

[47] R. Tibshirani, "Regression Shrinkage and Selection via The Lasso: A Retrospective," *Journal of the Royal Statistical Society Series B: Statistical Methodology*, vol. 73, no. 3, pp. 273–282, 04 2011.

[48] S. Boyd, N. Parikh, E. Chu, B. Peleato, and J. Eckstein, "Distributed optimization and statistical learning via the alternating direction method of multipliers," *Found. Trends Mach. Learn.*, vol. 3, no. 1, p. 1–122, jan 2011. [Online]. Available: https://doi.org/10.1561/2200000016

[49] B. Ottersten, M. Viberg, P. Stoica, and A. Nehorai, *Exact and Large Sample Maximum Likelihood Techniques for Parameter Estimation and Detection in Array Processing*. Berlin, Heidelberg: Springer Berlin Heidelberg, 1993, pp. 99–151.